



HAL
open science

Angular and radial sampling criteria for monostatic and bistatic radar tomography of solar system small bodies

Mark S. Haynes, Ines Fenni, Yonggyu Gim, Wlodek Kofman, Alain Herique

► To cite this version:

Mark S. Haynes, Ines Fenni, Yonggyu Gim, Wlodek Kofman, Alain Herique. Angular and radial sampling criteria for monostatic and bistatic radar tomography of solar system small bodies. *Advances in Space Research*, 2021, 68, pp.3903-3924. 10.1016/j.asr.2021.07.035 . insu-03705265

HAL Id: insu-03705265

<https://insu.hal.science/insu-03705265>

Submitted on 27 Jun 2022

HAL is a multi-disciplinary open access archive for the deposit and dissemination of scientific research documents, whether they are published or not. The documents may come from teaching and research institutions in France or abroad, or from public or private research centers.

L'archive ouverte pluridisciplinaire **HAL**, est destinée au dépôt et à la diffusion de documents scientifiques de niveau recherche, publiés ou non, émanant des établissements d'enseignement et de recherche français ou étrangers, des laboratoires publics ou privés.



Distributed under a Creative Commons Attribution - NonCommercial - NoDerivatives 4.0 International License



Angular and radial sampling criteria for monostatic and bistatic radar tomography of solar system small bodies

Mark S. Haynes^{a,*}, Ines Fenni^a, Yonggyu Gim^a, Wlodek Kofman^{b,c}, Alain Hérique^b

^a Jet Propulsion Laboratory, California Institute of Technology, 4800 Oak Grove Dr., Pasadena, CA 91109, USA

^b Univ. Grenoble Alpes, CNRS, CNES, IPAG, Grenoble, France

^c Centrum Badan Kosmicznych Polskiej Akademii Nauk (CBK PAN), PL-00-716 Warsaw, Bartycka 18A, Poland

Received 12 February 2021; received in revised form 24 June 2021; accepted 27 July 2021

Available online 5 August 2021

Abstract

Low-frequency radar tomography is an important subsurface imaging method for future planetary missions to solar system small bodies. We derive angular and radial sampling criteria for monostatic and bistatic radar tomography algorithms that are based on monochromatic free-space backprojection and spherical apertures. We use the vector Born approximation to highlight the degeneracy of monochromatic bistatic source/receiver direction pair measurements in k -space. Analytical expressions are then derived for the scalar point target response of different spherical sampling geometries. We also derive the angular sampling step and total number of sampling points required to fully reconstruct the point target response for monostatic, bistatic, and non-degenerate k -space spherical apertures. These are evaluated for object sizes and radar operating frequencies expected in small body tomography. We also analyze and derive expressions for the coherence loss of spherical apertures due to random errors in a sensor's radial position, which provides requirements on the a posteriori ephemeris knowledge. Finally, we derive a vector backprojection algorithm suitable for focusing quad-pol scattering matrix (S-matrix) data that is tested using full-wave S-matrix simulations of dielectric point targets. This work is intended to aid radar instrument performance analysis and inform the design and architecture of future instruments and missions.

© 2021 COSPAR. Published by Elsevier B.V. This is an open access article under the CC BY-NC-ND license (<http://creativecommons.org/licenses/by-nc-nd/4.0/>).

Keywords: Radar; Tomography; Solar system small bodies; Point target response; Born approximation; Sampling criteria

1. Introduction

Radar tomography is the most promising method to remotely image the interior of solar system small bodies, [Kofman and Safaeinili \(2004a\)](#), [Safaeinili et al. \(2002\)](#), [Hérique et al. \(2018\)](#), [Haynes et al. \(2020\)](#). By collecting reflection and transmission radar measurements around a small body, tomographic radar processing can be used to form 3D images of the interior structure or dielectric constant of asteroids or comets. Rosetta-CONSERT, [Kofman et al. \(2007\)](#); [Kofman et al. \(2015\)](#); [Hérique et al. \(2016\)](#),

was the first of its kind to take limited transmission measurements through the nucleus of comet 67P/C-G. The CORE mission was proposed as a NASA Discovery-class to perform comprehensive monostatic imaging of comet 10P/Tempel 2, [Asphaug et al. \(2014\)](#). The only radar currently being developed for asteroid imaging will be part of the Hera mission to the asteroid Didymos, [Michel et al. \(2018\)](#), which will carry the Juventus cubesat, [Goldberg et al. \(2019\)](#); JuRa will be a monostatic and full polarization radar sounder at 60 MHz to probe the smaller asteroid of the binary pair, [Herique et al. \(2020\)](#). Smallsat and cubesats missions and radar hardware are or have been proposed for monostatic and bistatic tomography, [Pursiainen and Kaasalainen \(2016\)](#); [Bambach et al.](#)

* Corresponding author.

E-mail address: mark.s.haynes@jpl.nasa.gov (M.S. Haynes).

(2018); Granados et al. (2018); Hérique et al. (2019). In general, these radar systems are in-family with traditional long-wavelength (HF) orbital radar sounders MARSIS, SHARAD, and LRS Picardi et al. (2004); Seu et al. (2007); Ono and Oya (2000) which use low frequencies in order to overcome absorption and scattering losses through rough surfaces.

There are three general categories of 3D imaging algorithms that can be used for small body interior imaging, Safaeinili et al. (2002). The first are free-space methods in which images of scattered intensity are formed by backprojecting scattered field measurements onto the image domain. These include radar tomography, Knaell and Cardillo (1995), 3D synthetic aperture radar (SAR), Gim et al. (2014); Arumugam et al. (2018), and reflection or diffraction tomography. Diffraction tomography, specifically, is derived under the Born approximation, where the spectral (k -space) components of an object are mapped to source/receiver direction pairs, Devaney (1984); Kofman and Safaeinili (2004b). The second category are inversions of average dielectric properties using kinematic properties of waves, e.g., speed of light, time delay, and attenuation. This method was used on Rosetta-CONSERT data, Kofman et al. (2015); Hérique et al. (2016). The third category are full-wave electromagnetic non-linear inverse scattering methods, Chew and Wang (1990); van den Berg et al. (1999); Haynes et al. (2012), in which the 3D dielectric of an object is found through an inversion process by matching forward model predictions to measurements. This has also been referred to as wavefield tomography, far-field inversion, or full-wave tomography Sava and Asphaug (2018b); Takala et al. (2018); Sorsa et al. (2019). Free-space methods are easier to analyze, but full-wave methods are ultimately required to maximize the science potential of radar echoes.

Key questions for the future design and development of small body radar tomography missions are: 1) what is the required angular sampling spacing between radar measurements around a small body, 2) what is the total number of spherical sampling points required for complete imaging of a small body, 3) how well do the locations of sensors need to be known? Understanding these is crucial because they drive orbit design and coverage, mission duration, requirements on reconstructed ephemeris accuracy, data volume, radar function and performance, and ultimately mission feasibility. Sampling criteria for far-field monostatic systems around small bodies was derived in Sava and Asphaug (2018a) using k -space arguments, and Pursiainen and Kaasalainen (2016) studied the effect of different bistatic sampling configurations on dielectric inversion of small body voids but a rationale for the angular sampling step was not given. The purpose of this work is to formally derive and study the angular and radial sampling criteria for free-space monochromatic 3D radar tomography in monostatic and bistatic spherical geometries in order to provide equations and rationale for radar system engineering and mission trade studies.

Three-dimensional tomographic radar systems in spherical apertures have theoretical image resolutions that are diffraction-limited, i.e., on the order of the wavelength. This differs from traditional linear SAR in which range and azimuth resolutions are restricted by the transmit bandwidth and synthetic aperture length. Diffraction-limited resolution applies to both backpropagation and inverse scattering methods, and is achievable with monochromatic radar systems (i.e., CW) when the full angular diversity of scattered field measurements are sampled. Monochromatic operation is an end member for both analysis and hardware design. In practice, radar systems with modest transmit bandwidth can reduce the required spatial sampling density compared to that needed for monochromatic systems. In effect, bandwidth permits more information per spatial sampling location. However, for narrowband systems, like those based on simple dipole antennas, monochromatic analyses are reasonable tools for first-order system assessments.

Finally, radar tomography is an inherently vector problem and must be considered in system analysis and imaging algorithms. Inverse scattering methods readily handle the vector nature of the data and scattering phenomenology. Most point target analysis and k -space methods, however, are derived for scalar scattering. In Section 2, we use the vector Born approximation to link vector fields to scalar scattering and k -space analysis. This is used to illustrate the degeneracy of bistatic wavevector combinations in k -space when different source/receiver pairs map to identical object spectral components. This degeneracy affects the count of the total number of required spherical sampling points. In Section 8 we derive a vector backprojection algorithm suitable for monochromatic focusing of quad-pol scattering matrix data. The algorithm is tested on simulated data of dielectric point targets in Section 9.

The rest of the paper is organized as follows. In Section 3 we derive analytical expressions for scalar point target responses for monostatic and bistatic sampling geometries. These are useful for general assessments of 3D apertures. In Section 4, we derive the angular sampling criteria for these geometries using SAR Doppler arguments and plane wave harmonic analysis. In Section 5 the sampling rates are used to predict the total number of angular sampling points needed to fully sample a spherical aperture for each geometry. The sampling criteria is validated in Section 6 in simulation. In Section 7, we analyze the effects of radial position errors on aperture coherence, which gives criteria on spacecraft position errors needed to successfully form 3D tomographic images. Finally, the implications of these results and their effect on future mission feasibility are discussed in Section 10.

2. Vector Born approximation, k -space

We use the vector Born approximation (BA) to derive the well-known relationship between the spatial spectrum, or k -space, of a dielectric object and the incident/scattered

wavevector directions. We use this to point out an important but lesser-known degeneracy of bistatic measurements in k -space which is a direct result of the BA. This degeneracy has implications for how we count of total number of bistatic measurements in Section 5. In general, the analytical vector equations derived under the BA do not apply to highly irregular, heterogenous, or lossy bodies because, in the presence of multiple scattering, there is not a one-to-one mapping between sensor position and the object spatial spectral components.

2.1. Vector Born approximation

The volume integral equation (VIE) for the scattered electric field for an inhomogeneous dielectric object is, [Chew \(1995\)](#)

$$\mathbf{E}_{sca}(\mathbf{r}) = \int \overline{\mathbf{G}}(\mathbf{r}, \mathbf{r}') \cdot \mathbf{O}(\mathbf{r}') \mathbf{E}(\mathbf{r}') dV' \quad (1)$$

where \mathbf{E} is the total field solution in the object, \mathbf{E}_{sca} is the scattered field outside of the object, $\overline{\mathbf{G}}(\mathbf{r}, \mathbf{r}')$ is the dyadic Green's function, and the object function is

$$\mathbf{O}(\mathbf{r}) = k^2(\mathbf{r}) - k^2 \quad (2)$$

where $k(\mathbf{r})$ is wavenumber in the object and $k = 2\pi/\lambda$ is the background wavenumber.

The three conditions of the Born approximation are:

1. Born approximation for the total field in the object, $\mathbf{E}(\mathbf{r}) = \mathbf{E}_{inc}(\mathbf{r})$,
2. Plane wave incidence, $\mathbf{E}_{inc}(\mathbf{r}) = E_o \hat{e}_i \exp(i\mathbf{k}_i \cdot \mathbf{r})$,
3. Far-field Green's function, [\(3\)](#).

The far-field approximation of the dyadic Green's function in the scattered field direction is

$$\overline{\mathbf{G}}(\mathbf{r}, \mathbf{r}') \approx [\mathbb{I} - \hat{r}\hat{r}] \frac{e^{ikr}}{4\pi r} e^{-i\mathbf{k}_s \cdot \mathbf{r}'} \quad (3)$$

Substituting these into [\(1\)](#), the Born approximation for the VIE is

$$\mathbf{E}_{sca}(\mathbf{r}) = \frac{e^{ikr}}{4\pi r} [\mathbb{I} - \hat{r}\hat{r}] \cdot \mathbf{E}_i \int \mathbf{O}(\mathbf{r}) e^{i(\mathbf{k}_i - \mathbf{k}_s) \cdot \mathbf{r}} dV \quad (4)$$

The volume integral has reduced to the 3D Fourier transform of the object function in the wavevector difference domain. This is the classical k -space relation between the scalar scattering of the object and the incident/scattered direction that map to the object spatial frequency components. A similar expression is derived in [Safaeinili et al. \(2002\)](#); [Eyraud et al. \(2013\)](#). Under the BA, scattering is purely scalar, there is no multiple scattering, and depolarization only appears as the projection between incident and scattered plane wave polarizations. The Born approximation assumes that the total field solution is unaffected by the object, and this is only valid when the objects are small compared to the wavelength and/or have low dielectric contrast.

Because the BA relies on plane waves, [\(4\)](#) can be cast as a scattering matrix, or S-matrix. In spherical coordinates, $\mathbb{I} - \hat{r}\hat{r} = \hat{\theta}_s \hat{\theta}_s + \hat{\phi}_s \hat{\phi}_s$, then decomposing the incident and scattered polarizations into \hat{v} and \hat{h} components, the far-field S-matrix can be written

$$\begin{bmatrix} E_{sv} \\ E_{sh} \end{bmatrix} = \frac{e^{ikr}}{4\pi r} \begin{bmatrix} S_{vv} & S_{vh} \\ S_{hv} & S_{hh} \end{bmatrix} \begin{bmatrix} E_{iv} \\ E_{ih} \end{bmatrix} \quad (5)$$

where

$$\begin{bmatrix} S_{vv} & S_{vh} \\ S_{hv} & S_{hh} \end{bmatrix} = \begin{bmatrix} \hat{v}_s \cdot \hat{v}_i & \hat{v}_s \cdot \hat{h}_i \\ \hat{h}_s \cdot \hat{v}_i & \hat{h}_s \cdot \hat{h}_i \end{bmatrix} \int \mathbf{O}(\mathbf{r}) e^{i(\mathbf{k}_i - \mathbf{k}_s) \cdot \mathbf{r}} dV \quad (6)$$

The unit wavevectors and polarizations are defined, [Tsang et al. \(2000\)](#),

$$\hat{k}_i = \sin \theta_i \cos \phi_i \hat{x} + \sin \theta_i \sin \phi_i \hat{y} + \cos \theta_i \hat{z} \quad (7)$$

$$\hat{v}_i = \cos \theta_i \cos \phi_i \hat{x} + \cos \theta_i \sin \phi_i \hat{y} - \sin \theta_i \hat{z} \quad (8)$$

$$\hat{h}_i = -\sin \phi_i \hat{x} + \cos \phi_i \hat{y} \quad (9)$$

$$\hat{k}_s = \sin \theta_s \cos \phi_s \hat{x} + \sin \theta_s \sin \phi_s \hat{y} + \cos \theta_s \hat{z} \quad (10)$$

$$\hat{v}_s = \cos \theta_s \cos \phi_s \hat{x} + \cos \theta_s \sin \phi_s \hat{y} - \sin \theta_s \hat{z} \quad (11)$$

$$\hat{h}_s = -\sin \phi_s \hat{x} + \cos \phi_s \hat{y} \quad (12)$$

where (θ_i, ϕ_i) and (θ_s, ϕ_s) are spherical angles. \hat{h} and \hat{v} are the same as $\hat{\theta}$ and $\hat{\phi}$ unit vectors in spherical coordinates and they form an orthogonal system with \hat{k} as shown in [Fig. 1](#).

Measuring the S-matrix requires a fully-polarimetric radar system. For low-frequency radar systems around an asteroid or comet, this can be accomplished with cross-dipole antennas and independent transmit and receive signal paths in the RF electronics. The above equations assume that the dipole antennas are oriented tangent to the sphere enclosing the object. In Section 8, we will derive a backprojection algorithm suitable for vector data based on sampling the full S-matrix.

2.2. k -space

Under the Born approximation, a bistatic pair of plane waves $(\mathbf{k}_i, \mathbf{k}_s)$ measures the object spectral component $\mathbf{k} = \mathbf{k}_i - \mathbf{k}_s$. This interpretation is well-known for all free-

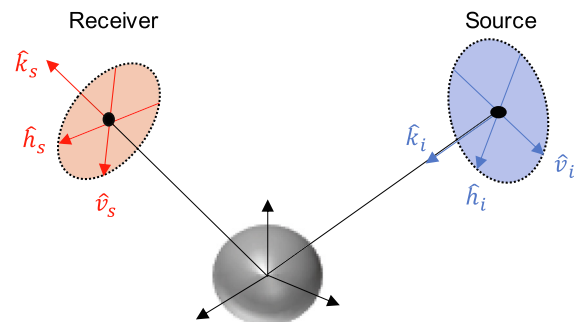


Fig. 1. Relation between wavevectors and polarization vectors.

space focusing or diffraction tomography algorithms, Devaney (1984); Kofman and Safaeinili (2004b). The main ideas are:

1. In the forward scattering convention, $-\hat{k}_i$ points to the source, and \hat{k}_s points to the receiver.
2. Monostatic measurements are any $\mathbf{k}_s = -\mathbf{k}_i$, where $\mathbf{k} = 2\mathbf{k}_i$. Monochromatic reflections sample a k -space sphere with radius $2k$. This is the highest spatial frequency that can be directly sampled by that probing frequency.
3. $\mathbf{k}_s = \mathbf{k}_i$ is pure transmission. All antipodal source/receiver pairs map to $\mathbf{k} = 0$ under the BA.
4. $\mathbf{k}_s \neq \mathbf{k}_i$ is a general bistatic measurement. If the source and receiver directions are reversed, $\mathbf{k}_i = -\mathbf{k}_s, \mathbf{k}_s = -\mathbf{k}_i$ the same k -space location is sampled. This is a statement of reciprocity.

These are illustrated in 3D in Fig. 2. Fig. 3 shows discrete k -space samples due to evenly spaced source/receive sampling around a circle in 2D. The outer circle (pink) are monostatic measurements, the inner circle (red) are fixed transmit, all receive measurements. Moving the transmitter (green) sweeps out the full set of bistatic measurements (blue dots) as a sum of fixed transmit geometries. The inner most circle (cyan) are near-transmission, and the center is pure antipodal transmission.

2.3. Degeneracy of bistatic measurements in k -space

A direct consequence of the BA and k -space formulations is the degenerate mapping of different incident/scattered wavevector combinations to the same object spectral component. Under the BA, any incident/scattered combinations that satisfy $\mathbf{k} = \mathbf{k}_i - \mathbf{k}_s$ are considered equivalent measurements, irrespective of the nature of the object. We explain this degeneracy in detail next.

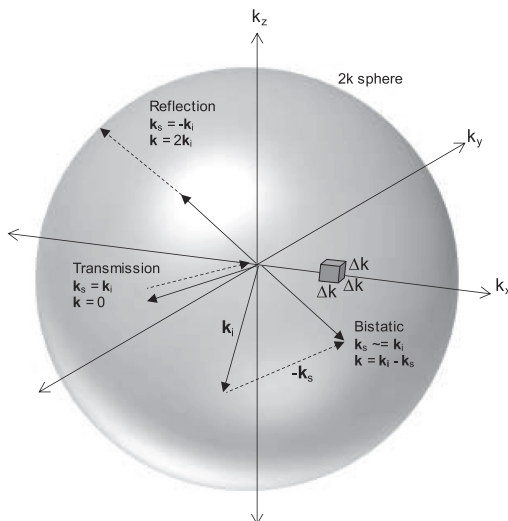


Fig. 2. 3D k -space spectral sampling for three source/receiver geometries.

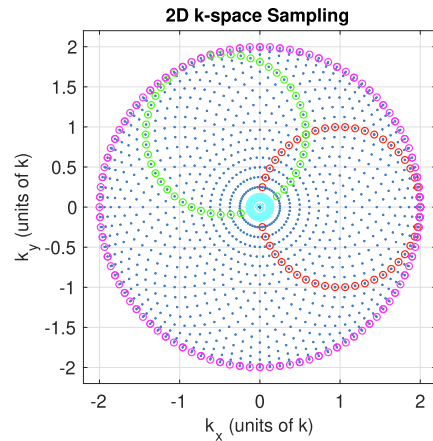


Fig. 3. 2D discrete k -space sampling due to circular geometry of sources and receivers.

In 2D, there are exactly two ways to sample the same k -space location with monochromatic waves. These are found by reversing an initial pair of incident/scattered wavevectors, and is the same as reflecting an initial head-to-tail path of the wavevectors over the resultant \mathbf{k} , shown in Fig. 4. In 3D, there are an infinite number of ways to sample the same k -space location with monochromatic waves. These are found by spinning the head-to-tail path of \mathbf{k}_i and $-\mathbf{k}_s$ about the resultant vector \mathbf{k} , shown in Fig. 4. Any pair of incident/scattered wavevectors that lie on the outside of the cones formed by this procedure map to the same \mathbf{k} . In other words, they appear to be the same measurement. In general, this is not true, especially for large, highly heterogeneous, or asymmetric dielectric objects.

In the spatial domain, the degeneracy can be understood geometrically as source/receiver pairs that fall on opposite sides of a circle that is formed by spinning an initial pair of source/receiver position unit vectors about their bisector, shown in Fig. 5. Every opposing source/receiver pair on any circle are reciprocal. All pairs on the same circle are degenerate in k -space.

The degeneracy of bistatic k -space measurements creates a problem for how we count the total number measurements for 3D tomography. One way to count the required

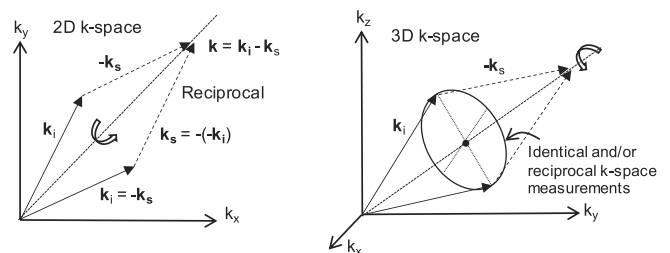


Fig. 4. Left: 2D reciprocal measurements that sample the same point in k -space. Right: Identical ways of sampling the same k -space location from pairs of bistatic measurements in 3D. This illustrates the degeneracy of bistatic measurements under the Born approximation and free-space k -space formulations.

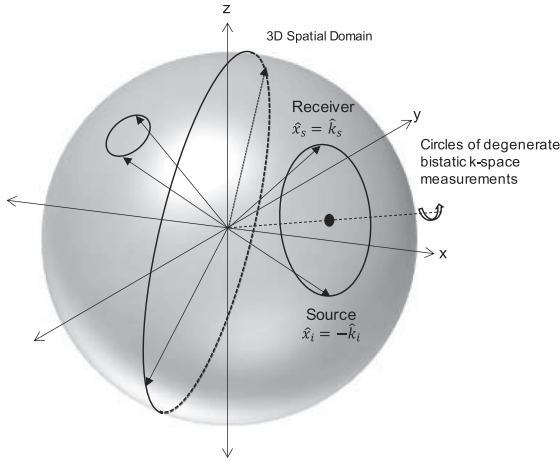


Fig. 5. Spatial domain representation of bistatic measurement degeneracy in k -space. The sphere represents source/receiver position unit vectors. Circles are created by rotating an initial pair of source/receiver position vectors about their bistector. All opposite bistatic pairs on any given circle map to the same \mathbf{k} of the object spectrum under the Born approximation.

number of bistatic measurements is to sample every \mathbf{k} exactly once. However, this predicts many fewer bistatic measurements than what is predicted by taking all possible combinations of bistatic directions for a given spherical sampling density. This will be discussed further in Section 5.

Finally, we only consider monochromatic waves in this work, but an additional degeneracy occurs in frequency where the combination of frequency and observation angle map to identical k -space locations. In this case, while the degeneracy of k -space appears to worsen, a system with finite bandwidth would lessen the required spatial sampling density because the same information could be obtained from fewer sensor positions.

The k -space degeneracy, whether for monochromatic or finite bandwidth systems, also has consequences for orbit design. Assuming the BA as a reasonable start point, we might choose an orbit solution such that k -space is sampled as quickly as possible with the least redundancy. Therefore, the extent to which degeneracy is avoided can be used as a possible metric for data collection efficiency.

3. Scalar 3D point target response

The point target response (PTR) is a fundamental metric for evaluating the performance and sampling requirements of an imaging system. The PTR gives the theoretical resolution of the backprojected image of an infinitesimal point target. We derive the PTR for monostatic, bistatic, fixed-transmit, and k -space sampling geometries for scalar waves in free-space. These allow us to discuss sampling and data acquisition strategies of 3D tomography under the BA in a way decoupled from the details of the object or radar instrument. Using the PTRs, we show that diffraction limited resolution is possible with monochromatic spherical apertures. In addition, we show how the bistatic PTRs

differ with and without the k -space degeneracy. The analytic results here will be used in Sections 4 and 7 to numerically validate the angular and radial sampling criteria for the sampling geometries.

3.1. Discrete scalar PTR

For a scalar source located in the far-field in direction $(\pi - \theta_i, \phi_i + \pi)$, an incident plane wave with unit amplitude is given by

$$\phi_{inc}(\mathbf{x}) = e^{i\mathbf{k}_i \cdot \mathbf{x}} \tag{13}$$

where $\mathbf{k}_i = k\hat{\mathbf{k}}_i$. The far-field scattered field of a unit-amplitude point target located at \mathbf{x}_p is

$$\phi_{sca,(i,s)} = e^{i(\mathbf{k}_i - \mathbf{k}_s) \cdot \mathbf{x}_p} \tag{14}$$

where (i, s) indexes an incident/scattered direction pair and

$\mathbf{k}_s = k\hat{\mathbf{k}}_s$. The scattered field of a point target is just the phase difference between the incident and scattered plane waves measured at the target relative to the origin. The monochromatic focused field (or voltage) image is founded by reradiating, or backprojecting, each scattered field measurement onto the imaging domain with conjugate phase and summing over all measurement pairs:

$$V = \sum_{(i,s)} \phi_{sca,(i,s)} e^{-i(\mathbf{k}_i - \mathbf{k}_s) \cdot \mathbf{x}} \tag{15}$$

Substituting (14) into (15), the 3D image of the point target response (PTR) is

$$V = \sum_{(i,s)} e^{-i(\mathbf{k}_i - \mathbf{k}_s) \cdot (\mathbf{x} - \mathbf{x}_p)} \tag{16}$$

Eq. (16) can be used to compute the PTR for any arbitrary collection of incident and scattered measurement direction pairs, under the assumptions of identical illumination (e.g., identical transmit power and antenna gain) and known source/receive position.

3.2. Scalar PTR with continuous sampling

The point target responses in (15) and (16) can be evaluated analytically in the limit of a continuous number of measurements. Letting $\mathbf{x}_p = 0$, the continuous version of (16) is

$$V = \int_{\Omega_s} \int_{\Omega_i} e^{-i(\mathbf{k}_i - \mathbf{k}_s) \cdot \mathbf{x}} d\Omega_i d\Omega_s \tag{17}$$

where the integrals are evaluated over the wavevector, or k -space, surfaces Ω . This is technically an integral over the 4D space of incident/scattered spherical directions. The differential area of each sphere is $d\Omega = k^2 \sin \theta d\theta d\phi$, where the angles are spherical angles in k -space. If a signal consists of multiple frequencies, or has finite bandwidth, the integral should be evaluated over the volumes of the incident and scattered wave numbers.

Full Monostatic. For a full monostatic, reflection-only sampling geometry, $\mathbf{k}_s = -\mathbf{k}_i$, (17) becomes an integral over one k -space sphere:

$$V_{mono} = \int_{\Omega_i} e^{-i2\mathbf{k}_i \cdot \mathbf{x}} d\Omega_i \quad (18)$$

Using the results in Appendix A, this evaluates to

$$V_{mono} = 4\pi k^2 \text{sinc}(2kr) \quad (19)$$

The PTR is a radial sinc function centered on the target where the first null-to-null width is equal to $\lambda/2$. When the entire sphere of reflected directions is collected, the PTR is diffraction limited. The scale factor, $4\pi k^2$, is the surface area of the k -space sphere with radius k , and is replaced by the number of reflected directions when computing the PTR from the discrete sum (16).

Full Bistatic. For a full bistatic geometry, all combinations of incident and scattered directions are collected, therefore (17) (and (16)) can be separated as

$$V_{bi} = \int_{\Omega_i} e^{-i\mathbf{k}_i \cdot \mathbf{x}} d\Omega_i \int_{\Omega_s} e^{i\mathbf{k}_s \cdot \mathbf{x}} d\Omega_s \quad (20)$$

Using Appendix A, this becomes

$$V_{bi} = (4\pi k^2)^2 \text{sinc}^2(kr) \quad (21)$$

The full bistatic PTR has a null-to-null width equal to λ and it has lower sidelobes than the monostatic PTR (19). The scale factor is squared due to the fact that all possible bistatic pairs of measurements are included in the acquisition. This includes all degenerate k -space pairs and can be considered an auto-convolution of the fixed transmit, all receive geometry (see next) over transmit directions.

Fixed Transmit, All Receive. When the incidence direction is fixed and all scattered directions are used, then the \mathbf{k}_i integral in (17) becomes constant and

$$V_{fixed} = e^{-i\mathbf{k}_i \cdot \mathbf{x}} \int_{\Omega_s} e^{i\mathbf{k}_s \cdot \mathbf{x}} d\Omega_s \quad (22)$$

which evaluates to

$$V_{fixed} = 4\pi k^2 e^{-i\mathbf{k}_i \cdot \mathbf{x}} \text{sinc}(kr) \quad (23)$$

This PTR has the widest width and the sidelobes levels are the same as the monostatic case. In addition, the incidence plane-wave phase is present in the PTR.

This case applies to measurement configurations where one sensor can be considered stationary and far away and a second sensor orbits the body. For example, the combination of a ground-based transmitter, high-altitude spacecraft, or celestial radio source with a low-altitude orbiting spacecraft. A lander-orbiter configuration is also in-family, but the PTR should be redefined due to the fact that the lander is in the near field of the object.

Full k -space. The point target response when k -space is fully sampled is given by the inverse Fourier transform over the spherical k -space volume. Here each \mathbf{k} is sampled exactly once out to a radius of $2k$. The PTR integral is

$$V_{k\text{-space}} = \int_0^{2k} \int_0^{2\pi} \int_0^\pi e^{-i\mathbf{k}' \cdot \mathbf{r}} dV'_k \quad (24)$$

where $dV_k = k^2 \sin \theta_k dk d\theta_k d\phi_k$. The integral over the spherical angles reduces to, Appendix A,

$$V_{k\text{-space}} = 4\pi \int_0^{2k} \text{sinc}(k'r) k'^2 dk' \quad (25)$$

which evaluates to

$$V_{k\text{-space}} = V_k \frac{3(\sin(2kr) - 2kr \cos(2kr))}{(2kr)^3} \quad (26)$$

where $V_k = 4\pi(2k)^3/3$ is the volume of the k -space sphere with radius $2k$. V_k multiplies a function with maximum value of one at $r = 0$. The multiplier, V_k , is replaced by the number of discrete samples had the PTR been computed as a discrete sum. Different from the full bistatic, this contains no degenerate measurement pairs. In addition, full bistatic sampling can be thought of as full k -space sampling with the addition of a weighting function that depends on the number of measurements contributing to the density of the degeneracy.

3.3. Comparison

Fig. 6 shows the point target responses for these acquisition geometries plotted as a function of radius from the center of the PTR. Table 1 gives numerical values for key properties. The 3 dB width of bistatic vs monostatic vs fixed transmit differ between them by approximately $\sqrt{2}$. In all cases, the 3 dB and 10 dB widths of the main lobe are $< \lambda$. Full bistatic resolution is roughly between $\lambda/3$ and $\lambda/2$. Full monostatic resolution is roughly between $\lambda/5$ and $\lambda/3$. The radius of the first sidelobe peak is found by differentiating the PTR analytically, (A.5), then solving for the zero numerically. The full k -space PTR has a side-

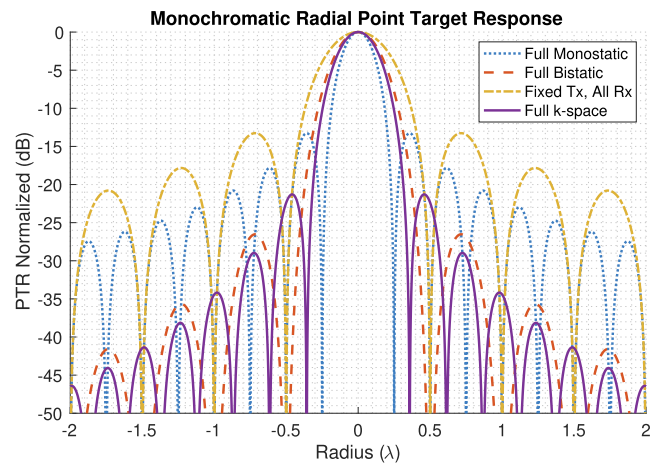


Fig. 6. Normalized radial point target response for monochromatic waves in free space for different sampling geometries.

Table 1
Properties of the free-space point target response of spherical apertures for different sampling geometries and monochromatic imaging.

3D Configuration	Normalized Radial PTR*	3 dB** width	10 dB** width	1 st null radius	1 st sidelobe radius	1 st sidelobe level
Full Monostatic	$\text{sinc}(2kr)$	0.2215λ	0.3690λ	$\lambda/4$	0.3576λ	-13.26 dB
Full Bistatic	$\text{sinc}^2(kr)$	0.3189λ	0.5570λ	$\lambda/2$	0.7151λ	-26.52 dB
Fixed Tx, all Rx	$\text{sinc}(kr)$	0.4429λ	0.7380λ	$\lambda/2$	0.7151λ	-13.26 dB
Full k -space	$\frac{3(\sin(2kr) - 2kr \cos(2kr))}{(2kr)^3}$	0.2888λ	0.4933λ	0.3576λ	0.4586λ	-21.29 dB

* PTR is a field (voltage) quantity. dB intensity (power) is computed with $20\log_{10}$. Note, $\text{sinc}(x) = \sin(x)/x$.

** Computed at linear powers of 0.5 and 0.1, respectively.

lobe envelope similar to full bistatic, but oscillates at a spatial frequency of $2k$ rather than k .

Designing or achieving specific sidelobe levels in the PTR is an important consideration for the design of the system. Weak targets can be ‘blinded’ by the sidelobes of strong targets. For example, in monostatic sampling, a target with a backscatter that is less than 30 dB below that of a nearby bright target will not be distinguishable in an image. The weakest desirable target sets an upper limit on the sidelobe levels. In classical SAR, range and azimuth sidelobe levels can be designed by a choice of weighting function in the fast-time and slow-time spectral domains. This classical approach could be generalized in 3D, where sampling strategy is treated as a k -space weighting function that is chosen to meet PTR sidelobe level requirements.

3.4. Analogue with linear SAR

The 3D geometries above have direct analogues with linear synthetic aperture radar (SAR), which is worth pointing out. Full monostatic is like traditional SAR in which the radar transmits and receives from the same location as the system moves. Full bistatic is analogous to a full phased array where all elements of an antenna array transmit and receive. Fixed transmit, all receive is analogous to passive SAR, where an external plane wave is incidence on a target and a linear aperture receives the echo. Like passive SAR, only the one-way phase contributes to the focusing and therefore the resolution is twice that of full monostatic. Full k -space is analogous to where the along-track SAR spectrum is sampled without degeneracy by a subset of partial phased array bistatic measurements. These are summarized in Table 2.

The traditional SAR along-track PTR can be found by replacing the argument of the analogous sinc functions for monostatic, bistatic, or fixed transmit, with

$$kr \rightarrow k \frac{L}{2} \sin \theta_{az} \quad (27)$$

where L is the synthetic aperture length and θ_{az} is the along track azimuth angle. The key distinction of spherical sampling geometries over traditional SAR is that diffraction-limited resolution is possible with monochromatic waves, while for linear SAR, the along track and range resolutions

Table 2
Linear SAR Analogs of 3D Sampling Geometries.

3D Sampling Geometry		SAR Analog
Full Monostatic	\leftrightarrow	Linear SAR
Full Bistatic	\leftrightarrow	Full Phased Array
Fixed Tx, all Rx	\leftrightarrow	Passive SAR
Full k -space	\leftrightarrow	Partial Phase Array

are limited by the synthetic aperture length and system bandwidth, respectively.

4. Angular sampling criteria

For small body tomography, one or more spacecraft are expected to fly near the body at a distance lower than a few tens of target radius Kofman et al. (2007); Michel et al. (2018). This configuration deviates significantly from Fraunhofer conditions in which optical rays are parallel Kong (1986) and waves incident the entire body as planes. Instead, for a given position of the two spacecrafts, each observed point of the target corresponds to different pairs of $(\mathbf{k}_i, \mathbf{k}_s)$. This means that the $(\mathbf{k}_i, \mathbf{k}_s)$ evolution of a point during a sequence of observations, which correspond to the Doppler history in SAR, depends on the position of the target relative to the spacecraft, Fig. 7.

The angular sampling criteria gives the maximum angular step between radar measurements that is needed in order to properly sample the phase of a target. Failing to meet the sampling criteria leads to side-lobes in the PTRs or aliasing in the object k -space. Sampling criteria for spherical apertures has been studied generally for SAR and near-field antenna systems, Fortuny-Guasch and Lopez-Sanchez (2001); Hansen (1988). The sampling criteria directly yields the total number of required measurements needed of fill out a spherical aperture. For small body radar tomography, this affects orbital coverage requirements, mission duration, as well as radar instrument operation, data rates and data volumes.

The angular sampling criteria for 3D tomography and spherical apertures can be derived several different ways. We do this first using arguments of traditional SAR Doppler. Second, we consider the convergence of the PTR at a given radius from the focal point. This sampling criteria will be used in Section 5 to compute the total number of

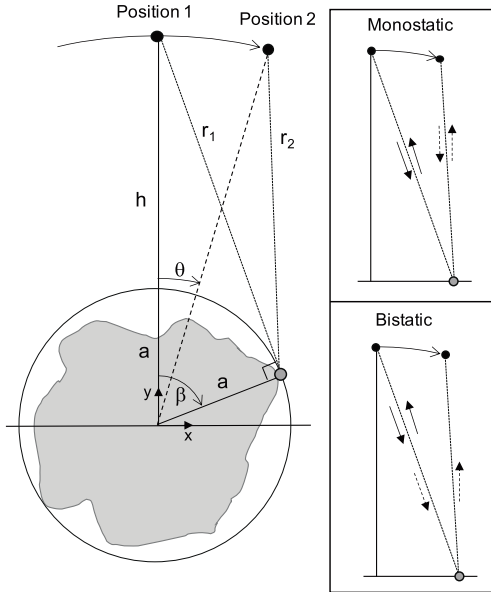


Fig. 7. Geometry for Doppler sampling and signal paths for computing the monostatic vs bistatic target phase differences on a spherically bound object.

sampling points. *k*-space sampling requirements are discussed in Section 5.2. In Sava and Asphaug (2018a), sampling criteria were derived for radiated plane waves using *k*-space arguments in the context of wavefield migration.

4.1. Doppler sampling

SAR Doppler deals with the rate of change of the target phase due to a change in sensor position, Richards et al. (2010). The Doppler frequency is usually given in terms of sensor velocity and look direction, but it fundamentally constrains the largest distance between two sensor positions required to Nyquist sample the target phase. For nadir-pointing planetary orbital radar sounders with near-omnidirectional antenna patterns, the maximum Doppler frequencies occur at the limbs. For small bodies, the limb is taken as the tangent to the body-enclosing sphere.

For monostatic operation, we must sample the difference of the two-way phase between two sensor positions. For bistatic or fixed-transmit operation, the ‘two-way’ phase consists of traversing the path once from one sensor to the target then to the second sensor. The geometry is shown in Fig. 7. Let the first sensor be on the *y*-axis at an altitude *h* above the body-enclosing sphere that has radius *a*. The second sensor position follows a circular orbit to an angle θ . The target is at the limb as viewed from the first sensor position. Exact expressions for the change in phase are given in Appendix B. Using those results, and assuming that $h/a > 0.2$ or $a > 2\lambda$, then the change in phase between sensor positions is well-approximated by

$$\Delta\phi_{2\text{-way,mono}} \approx 2ka \sin \theta \approx \frac{4\pi a}{\lambda} \theta \tag{28}$$

$$\Delta\phi_{2\text{-way,bi}} \approx ka \sin \theta \approx \frac{2\pi a}{\lambda} \theta \tag{29}$$

The Nyquist criteria is satisfied when $\Delta\phi$ is sampled faster than half a cycle, or $\Delta\phi_{2\text{-way}} \leq \pi$. The angular sampling step, $\Delta\theta$, between any two adjacent points is therefore

$$\Delta\theta_{\text{mono}} \leq \frac{1}{4} \frac{\lambda}{a} \tag{30}$$

$$\Delta\theta_{\text{bi}} \leq \frac{1}{2} \frac{\lambda}{a} \tag{31}$$

measured in radians. These only depend on the electrical size of the object and are independent of *h*. The angular sampling step of bistatic is twice that of monostatic, even though the total number of possible measurement pairs is much larger. For wide-bandwidth radar signals, the highest frequency (smallest wavelength) in the band should be used. For narrow-band signals, the wavelength of the center frequency is sufficient. (30) and (31) are plotted in Fig. 9 as a function of body diameter.

Eqs. (30) and (31) are consistent with the sampling criteria derived in Sava and Asphaug (2018a) which was done for one-way radiated plane waves. In particular, Sava and Asphaug (2018a, Eq. 8) is stated in terms of a spatial sampling step and maximum look angle. Exchanging the spatial step for the body radius, and the look angle for the angular step, we arrive at the same sampling criteria. The monostatic sampling differs by a factor of 2, which comes from one-way versus two-way accounting.

4.2. PTR convergence

A second way to derive the angular sampling criteria for free-space monochromatic focusing and spherical apertures is to require that the computation of the PTR sum (16) converge across the largest dimension of the object. That is, we want the PTR sidelobes for a focal point on one side of the object to converge to their theoretical values on the far-opposite side of the target. The geometry for this is shown in Fig. 8. The radius of convergence, r_c , needs to be equal to the largest diameter of the object. r_c depends on the total number of measured plane wave directions, and therefore their angular spacing, in (16).

The PTR radius of convergence is derived by considering the spherical harmonic content of the scalar plane wave expansion at a radius r_c measured from center of the focal point combined with the rules for quadrature integration of the Fourier surface integrals of the PTRs. Details are given in Appendix C. Setting the radius of convergence in (C.6) equal to the diameter of the body, $r_c = d = 2a$, the angular sampling steps to ensure PTR convergence in monostatic and bistatic geometries are

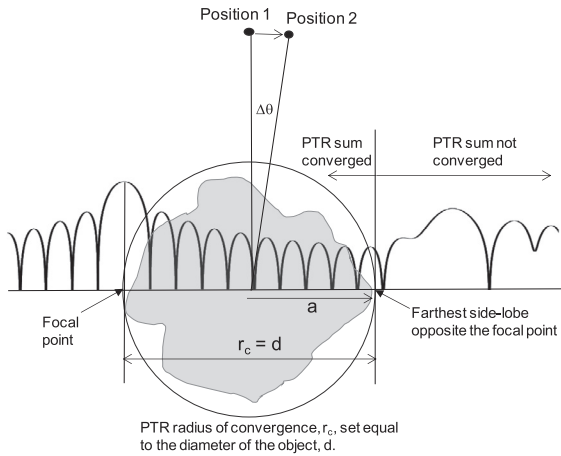


Fig. 8. Geometry showing the PTR radius of convergence, r_c , which needs to be equal to the body diameter, d .

$$\Delta\theta_{mono} \leq \frac{1}{4.4} \frac{\lambda}{a} \quad (32)$$

$$\Delta\theta_{bi} \leq \frac{1}{2.2} \frac{\lambda}{a} \quad (33)$$

This is finer sampling than the exact Doppler Nyquist limit (30), (31). The multiplier 1/1.1 acts like a Doppler over-sampling factor, but it is rigorously linked to the fidelity of the PTR via harmonic analysis. (32) and (33) are plotted in Fig. 9.

5. Total number of spherical sampling points

The total number of required spherical measurement points for 3D tomography is a critical metric for future radar tomography missions. It gives the coverage requirements that drive orbit design, data rate and volume, mission duration, and ultimately the trade between performance and mission feasibility. We use the angular sampling criteria above to count the total number of required measurements for monochromatic full monostatic

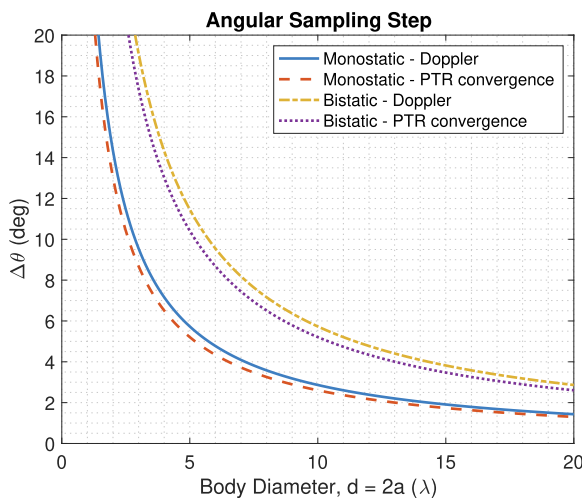


Fig. 9. Maximum required angular sampling step for monostatic and bistatic geometries, (30)–(33).

and full bistatic sampling. In this section, we also give the sampling criteria for non-degenerate full k -space sampling.

5.1. Number of monostatic and bistatic spherical sampling points

Assume that discrete plane wave directions are evenly distributed over the sphere according to the angular sampling criteria above. It is not necessary to take radar measures at exactly these sampling points. The plane wave directions need to be observed within $\Delta\theta/2$ of a prescribed direction on average in order to maintain the angular sampling rate in any direction around the sphere. An incident/scattered measurement pair is considered sampled if both the incident and scattered directions land within a small circular region on the sphere with area

$$\Delta\Omega \approx \pi \left(\frac{\Delta\theta}{2} \right)^2 \text{ sr} \quad (34)$$

The number of sampling points evenly distributed over the sphere is then

$$N = \frac{4\pi}{\Delta\Omega} \quad (35)$$

Substituting the Doppler sampling limits, (30), (31) into (34), and then into (35), the total number of sampling points required for full monostatic and full bistatic sampling are

$$N_{mono} = 4^4 \left(\frac{a}{\lambda} \right)^2 \quad (36)$$

$$N_{bi} = 4^3 \left(\frac{a}{\lambda} \right)^2 \quad (37)$$

The density of spherical sampling points goes as the square of the electrical dimension of the object, and the density of full bistatic is 1/4 that of full monostatic. (36) is plotted in Fig. 10 as a function of the object electrical

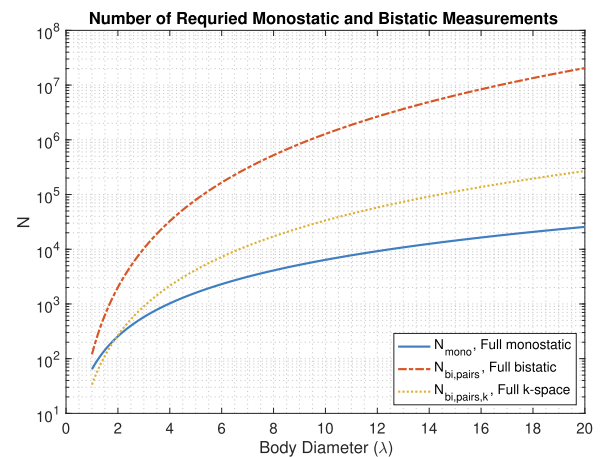


Fig. 10. Number of sampling points and bistatic measurements over the sphere for monostatic and bistatic geometries as a function of body diameter. The number of bistatic measurement pairs predicted from k -space sampling, $N_{bi,pairs,k}$, is much smaller than that predicted by pair-wise combination of Doppler-sampled bistatic points, $N_{bi,pairs}$.

diameter, and plotted again in Fig. 11 as a function of physical diameter and operating frequency. If (32) and (33) are used, then the numbers of points are about 20% larger.

For full monostatic, every plane wave direction only needs to be sampled once. For full bistatic, we count all possible pairs of incident/scattered directions for a given sampling. Using reciprocity, and excluding self-terms, the

number of unique Doppler-sampled bistatic measurement pairs given N_{bi} points distributed over the sphere is

$$N_{bi,pairs} = \binom{N_{bi}}{2} = \binom{N_{mono}/4}{2} \quad (38)$$

This is plotted in Fig. 10 and then in Fig. 11 as a function of operating frequency and body diameter. $N_{bi,pairs}$ goes as $\sim N_{bi}^2 \sim (a/\lambda)^4$. This grows very fast with an increase in body diameter or decrease in wavelength. Part of the reason for this growth is that (38) contains all possible degenerate bistatic pairs. It is so large, in fact, it seems implausible these points could be completely sampled by a realistic bistatic radar system. However, all of these spatial pairs are likely not required, discussed further Section 10.4.

5.2. Number of k -space sampling points

The number unique k -space points that are needed to Nyquist sample an object's spatial spectrum is also determined by the object size and operating wavelength. Due to the bistatic degeneracy in k -space, the total number of bistatic pairs that can fill out k -space is much smaller than that predicted by (38). The number of monostatic measurements turns out to be the same as (36).

The minimum number of k -space samples is found by dividing a k -space sphere of radius $2k$ by the volume of the 3D k -space voxel required to Nyquist sample an imaging domain. The highest measurable wavenumber is $2k$. The spectrum is two-sided, so the available spatial bandwidth is $4k$, which corresponds to a spatial sampling frequency, $f_x = 4/\lambda$ (this is consistent with Doppler sampling of a reflected wave at intervals of $\lambda/4$). The number of samples across the diameter of the object, d , is $N = f_x d$. The k -space step, Δk , is then equal to the spatial bandwidth divided by the total number of sample points

$$\Delta k = \frac{4k}{N} = \frac{2\pi}{d} \quad (39)$$

Due to the circulant property of the discrete Fourier transform in Cartesian coordinates, under this sampling, a point on one side of the object will be wrapped to the exact opposite side along the principal axes of the image. The volume of the k -space sphere is

$$V_k = \frac{4}{3} \pi (2k)^3 \quad (40)$$

The total number of cubic voxels of volume $V_{\Delta k} = (\Delta k)^3$ in V_k is

$$N_{bi,pairs,k} = \frac{V_k}{V_{\Delta k}} \quad (41)$$

$$= \frac{4}{3} \pi 4^3 \left(\frac{a}{\lambda}\right)^3 \quad (42)$$

$$= \frac{V}{(\lambda/4)^3} \quad (43)$$

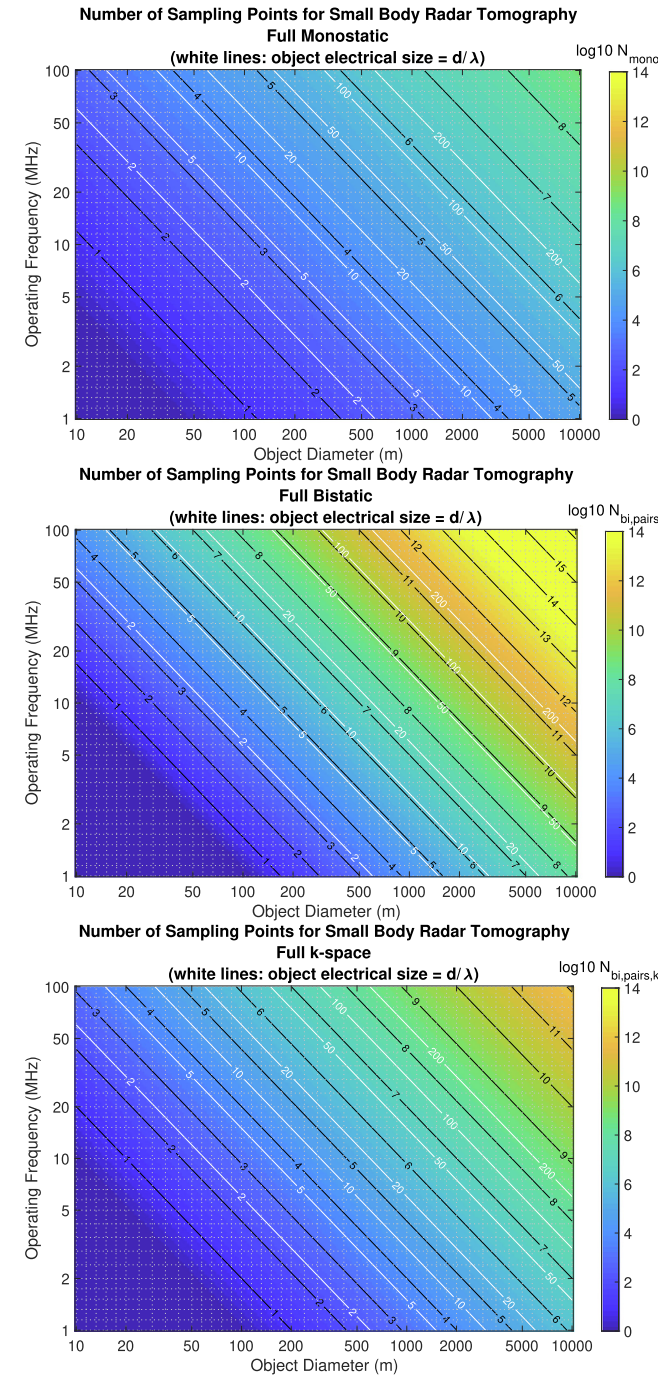


Fig. 11. Top: Number of monochromatic monostatic sampling points, N_{mono} , (36), on the sphere as a function of body diameter and operating frequencies that are in the typical range for radar tomography of solar system small bodies. Middle: Number of bistatic combinations, $N_{bi,pairs}$, (38). Bottom: Number of full k -space bistatic combinations, $N_{bi,pairs,k}$, (42).

where $d = 2a$ is the diameter of the imaging volume, V . (43) shows that the number of k -space samples is equal to the number of $\lambda/4$ cubes that fit in the volume of the spherical imaging domain. Because there are no degenerate k -space pairs, $N_{bi,pairs,k}$ is much smaller than (38). On the other hand, uniform k -space sampling does not easily map to a prescribed angular sampling criteria. Eq. (42) is shown in Fig. 11 as a function of operating frequency and object diameter.

The number of monostatic measurements is found by dividing the surface area of the $2k$ -radius sphere by an area $S_{\Delta k} = \pi(\Delta k/2)^2$, which is the disk-equivalent area of the side of a k -space 3D voxel. The surface area of the $2k$ -radius sphere is

$$S_k = 4\pi(2k)^2 \quad (44)$$

The number of points for monostatic acquisition in k -space is

$$N_{mono,k} = \frac{S_k}{S_{\Delta k}} \quad (45)$$

$$= 4^4 \left(\frac{a}{\lambda}\right)^2 \quad (46)$$

$$= \frac{S}{\pi(\lambda/4)^2} \quad (47)$$

where S is the surface area of the enclosing sphere. Eq. (46) is the same as that derived from the Doppler sampling (36). $N_{mono,k}$ is also equal the number of $\lambda/4$ -radius disks that divide the surface area of the enclosing sphere.

5.3. Relationship between k -space and full bistatic sampling

Bistatic measurements can be thought of as sampling a 4-dimensional space of spherical angles that describe the vectors $\mathbf{k}_i(\theta_i, \phi_i)$ and $\mathbf{k}_s(\theta_s, \phi_s)$. This has a mapping to k -space as: $\mathbf{k}(r_k, \theta_k, \phi_k, \gamma)$, which consists of the three dimensions of the k -space spherical volume (r_k, θ_k, ϕ_k) , plus a fourth dimension for the rotation of degenerate measurements, γ , about \mathbf{k} . This reduction in dimensionality between full bistatic and full k -space helps explain the dramatic decrease in the number of sampling points from $N_{bi,pairs}$, (38), to $N_{bi,pairs,k}$, (42).

6. PTR examples

We validate the angular sampling criteria and required number of sampling points by comparing the PTRs computed with the sum (16) with the analytic expressions. Source/receiver directions are arranged on the unit sphere using the disco ball approximation: points are distributed mostly evenly at discrete latitudes centered on a prime meridian, shown in Fig. 12. In this example there are 20 lines of latitude, which gives $N_{mono} = 478$ monostatic sampling directions, and $N_{bi,pairs} = 114,003$ bistatic combinations. The PTRs are computed along random radial lines through the center of the focal point, including the princi-

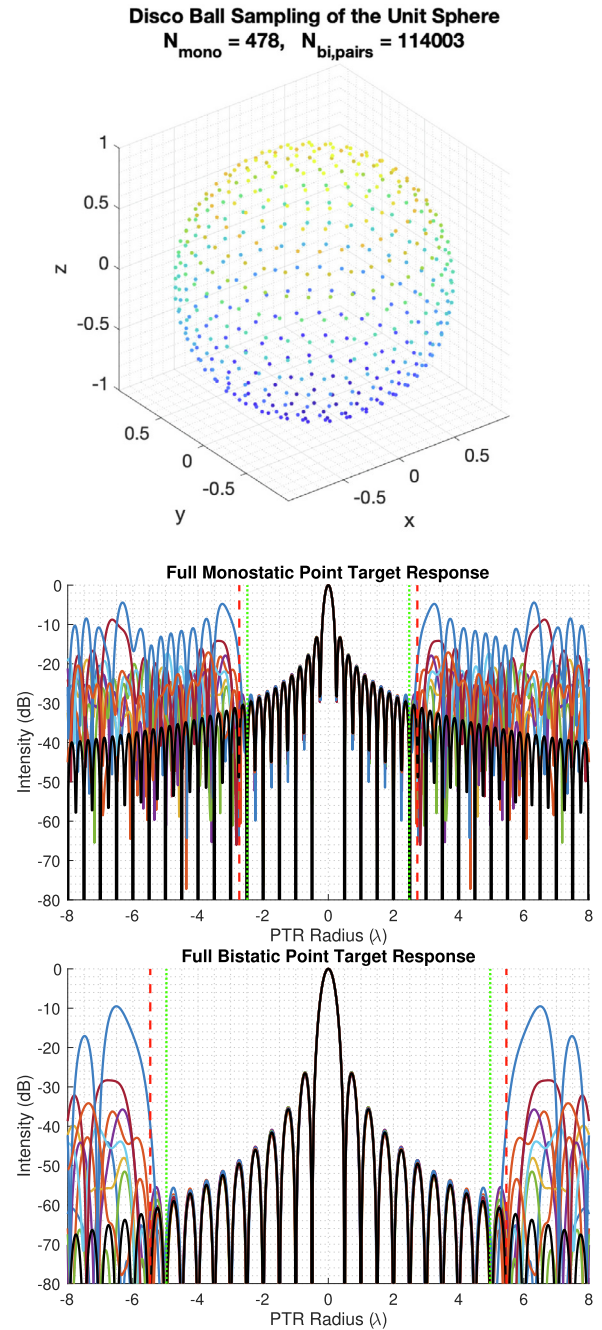


Fig. 12. Top: Disco ball sampling of source/receiver directions over the unit sphere. Middle: full monostatic PTR computed from (16) with $N_{mono} = 478$ measurement directions as random linear cuts through the origin (all lines). Bottom: full bistatic PTR computed from (16) with $N_{bi,pairs} = 114,003$ measurements at the same cuts. Analytical solution overlaid (solid black). The radii (i.e., object diameter) at which the PTR is predicted to converge for these numbers of measurements is shown for Doppler sampling (vertical red dashed lines) and PTR convergence criteria (vertical green dotted lines). Note, the radius of convergence of full bistatic PTR is twice that of full monostatic for the same spherical sampling density of points, albeit using a much larger number of measurement pairs.

pal axes of the imaging domain and plotted in Fig. 12. Overlaid are the analytic expressions, (19) and (21). The

results agree very well out to the radius of convergence, beyond which the PTRs do not converge.

Using (36) and (37), we solve for the diameter of the body for which the PTRs should converge given this number of sampling points, recalling that the body diameter is equal to the radius of convergence. The radius of convergence from Doppler Nyquist sampling, Section 4.1, is plotted as the vertical red dashed line, and that derived from harmonic analysis, Section 4.2, is plotted as the vertical green dotted line. Harmonic analysis better predicts the radius of convergence than the exact Doppler limit. In this example, the radius of convergence (body diameter) is about 2.5λ for full monostatic, and about 5λ for full bistatic. The radius of convergence of the full bistatic PTR is twice that of the full monostatic for the same spherical sampling density of plane waves, because the angular sampling requirement for full bistatic is half that of full monostatic, however, all combinations of bistatic measurements are needed.

The disco ball spacing probably cannot be sampled exactly in a real experiment where polar orbits around a small body are practical. The realized sampling will affect the PTR, especially when regions of the sphere are over- or under-sampled relative to the desired Doppler rate. Uneven sampling is analogous to a non-uniformly weighted linear antenna arrays, where the weighting affects the sidelobe structure of the PTRs. For example, if each point can be sampled within half the angular sampling step of the disco ball arrangement, then the sidelobes of the PTRs are bounded by a floor relative to the uniform spherical sampling. This has been confirmed numerically for the monostatic example in Fig. 12, where the sidelobe floor is about -25 dB. This effect is consistent with gradating lobe mitigation in randomly spaced linear antenna arrays.

Next, we validate the k -space sampling criteria. For comparison, we pick the object diameter to be equal to the radius of convergence for full bistatic in the example above, $d = 5\lambda$, where $\Delta k = 2\pi/d = 1.26/\lambda$. Using (42) this gives $N_{bi,pairs,k} = 4,169$ total k -space sampling points on a Cartesian grid within a radius of $2k$, shown in Fig. 13 (top). While FFT methods can be used, we compute the PTR using (16). For each k -space sample we find one corresponding incident/scattered wavevector pair. This is done by computing an arbitrary perpendicular vector, \mathbf{v} , to each \mathbf{k} , which originates from $\mathbf{k}/2$ such that $|\mathbf{k}_i| = |\mathbf{k}_s| = k$. \mathbf{k}_i and \mathbf{k}_s are the difference vectors between the resultant, $\mathbf{v} + \mathbf{k}/2$, and either the origin or \mathbf{k} , respectively. This procedure guarantees that all discrete \mathbf{k} are mapped to exactly one pair of bistatic measurements.

The full k -space PTR is computed along the same radial lines as those used in Fig. 12. The result is shown in Fig. 13 (bottom), where the analytical result (26) is overlaid (solid black). The match is good over a span of d , but not perfect, which is likely due to the Cartesian sampling of the k -space spherical volume. Images of the main lobe occur at $\pm 5\lambda$ along the XYZ axes, which are the circulant images that

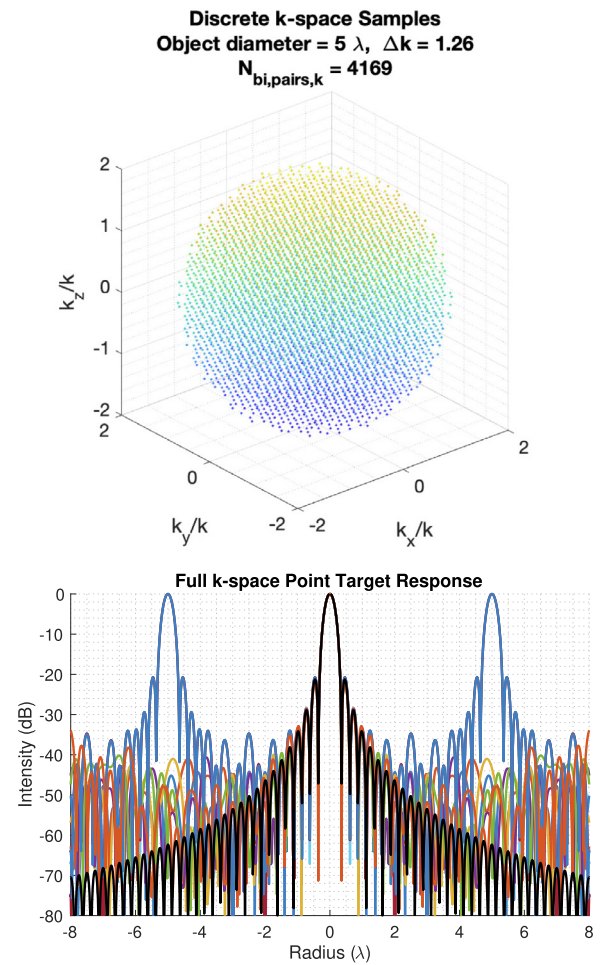


Fig. 13. Top: Discrete k -space samples on a Cartesian grid. Bottom: Full k -space PTR for a object dimension $d = 5\lambda$. Overlaid is the analytical results (26) and match is fairly good over a span of length d . The same cuts are used as those in Fig. 12. The PTR is replicated every d in XYZ due to the circulant properties of Cartesian k -space sampling.

occur every d due to the Cartesian sampling of \mathbf{k} . If the image diameter were doubled, and so Δk halved, the peaks would replicate every 10λ . The replication length in k -space is that same as the radius of convergence in the previous cases. Also, a different random set of non-degenerate incident/scattered directions produces the exact same discrete PTR, which is a direct consequence of the k -space degeneracy. This would not be the case when imaging real heterogeneous objects in which degenerate pairs in k -space give different scattered field measurements.

7. Radial position knowledge

It is generally accepted that the position of a radar sensor must be known to better than $\lambda/10$ to accurately focus radar echoes and create tomographic images. Small phase errors in the backprojected data lead to rapid coherence loss, or decoherence, of the focused field, which degrades the image and results in a loss of aperture gain. We derive

equations for the coherence loss of spherical apertures for monostatic and bistatic radar tomography. These equations are important for future mission design because they drive requirements on the uncertainty of the a posteriori reconstructed spacecraft ephemeris.

A complete treatment of this problem starts by giving each sensor a 3D position error, converting the position error to an equivalent phase error along the line of sight to the focal point, and then evaluating the ensemble average of the PTR power. For spherical apertures and far-field assumptions, the dominant effect is due to radial position errors. The same error projected in the angular direction has less impact. Coherence loss has been studied previously for linear synthetic apertures, [Greene and Moller \(1962\)](#), formation flying radar sounders, [Carrer et al. \(2019\)](#), and is the same phenomenon as rough surface backscatter loss under the Kirchhoff approximation, [Tsang et al. \(1985\)](#).

We derive the coherence loss for spherical apertures by studying the PTR sum (16) with zero-mean, uncorrelated Gaussian random phase errors. In practice, ephemeris smoothing or interpolation will lead to correlated position errors up to some spatial lag. Uncorrelated errors, though, provide useful insight and tools for quick performance trades.

7.1. Full monostatic

The coherence loss for monostatic sampling geometries due to errors in radial position knowledge is derived by starting with the discrete PTR sum (16), with $\mathbf{k} = \mathbf{k}_i = -\mathbf{k}_s$, the focal point $\mathbf{x}_p = 0$, and N sensors evenly distributed over a sphere. Each sensor has a radial position error, r_n , which counts twice toward the plane wave phase error, $2kr_n$. Each r_n is a zero-mean IID Gaussian random variable with standard deviation σ_r . The backprojected voltage is then

$$V = \sum_n e^{i2\mathbf{k}_n \cdot \mathbf{x}} e^{i2kr_n} \quad (48)$$

The average power is computed as the ensemble average over the magnitude-squared voltage

$$P = |V|^2 = VV^* \quad (49)$$

The analytic solution of the ensemble average is derived in [Appendix D](#). Using those results and notation, we identify $\psi_m = e^{i2\mathbf{k}_m \cdot \mathbf{x}}$, $|\psi_m| = 1$, $s = 2k$, and $\sigma = \sigma_r$, which gives an average power of

$$P = e^{-4k^2\sigma_r^2} P_c + \left(1 - e^{-4k^2\sigma_r^2}\right) P_i \quad (50)$$

$$P_c = N^2 \text{sinc}^2(2kr) \quad (51)$$

$$P_i = N \quad (52)$$

where P_c is the coherent PTR power of the unperturbed aperture (proportional to the square of the voltage PTR and scales as N^2), and P_i is the incoherent component of

the power due to random position errors (proportional to the number of sensors in the aperture, N). The exponential dependence on σ_r in (50) is similar to the backscatter coherence loss over random rough surfaces derived under the Kirchhoff approximation.

7.2. Full bistatic

The coherence loss for bistatic geometries due to radial position errors is also derived by starting with (16). For simplicity, we assume that each wavevector direction is associated with an independent source or receiver, i.e., there are no true monostatic measurements. This is the same as having a sphere of radius r_1 on which the source moves, and a sphere of radius r_2 on which the receiver moves, where $r_1 \neq r_2$. Each incident/scattered wavevector gets an independent random phase. This is done for analytical convenience. Were we to include true monostatic measurements, we would need to account for a two-way phase error at N monostatic points, while the roughly N^2 bistatic sensor pairs would have uncorrelated one-way phase errors. The expression for coherence loss would need to be rederived. However, we expect the difference between these two cases to be small, because the number of monostatic measurements is small compared to the set of bistatic combinations.

Both measurements of a reciprocal pair are included in the computation. We further assume that the spheres of measurement directions are equally well-sampled: there are N_m incident directions, N_n scattered directions, where $N_m = N_n = N$. The voltage PTR with random phases is then

$$V = \sum_{m,n} e^{i(\mathbf{k}_m - \mathbf{k}_n) \cdot \mathbf{x}} e^{ik(r_m + r_n)} \quad (53)$$

where (m, n) indexes an incident and scattered direction pairs, and r_m and r_n are zero mean IID Gaussian random variables. The sign of the random phase does not matter because the Gaussian distribution is symmetric. Because all bistatic pairs are measured independently, the double sum can be separated and the ensemble average distributed, so that (49) becomes

$$P = \left| \sum_m e^{i\mathbf{k}_m \cdot \mathbf{x}} e^{ikr_m} \right|^2 \left| \sum_n e^{-i\mathbf{k}_n \cdot \mathbf{x}} e^{ikr_n} \right|^2 \quad (54)$$

$$= \left| \sum_m e^{i\mathbf{k}_m \cdot \mathbf{x}} e^{ikr_m} \right|^2 \left| \sum_n e^{-i\mathbf{k}_n \cdot \mathbf{x}} e^{ikr_n} \right|^2 \quad (55)$$

Using the results and notation from [Appendix D](#), we identify $\psi_m = e^{i\mathbf{k}_m \cdot \mathbf{x}}$, $|\psi_m| = 1$, $s = k$, and $\sigma = \sigma_r$, and (55) becomes

$$P = \left(e^{-k^2\sigma_r^2} \sqrt{P_c} + \left(1 - e^{-k^2\sigma_r^2}\right) \sqrt{P_i} \right)^2 \quad (56)$$

$$P_c = N^4 \text{sinc}^4(kr) \quad (57)$$

$$P_i = N^2 \quad (58)$$

where P_c is the total coherent power of the full bistatic aperture (i.e., proportional to the bistatic PTR squared, which goes as N^4), and P_i is the total incoherent power (which goes as N^2). The squared roots in (56) account for the fact that in (54) we implicitly divided each bistatic voltage measurement evenly between the two sums. Expanding (56)

$$P = e^{-2k^2\sigma_r^2}P_c + 2e^{-k^2\sigma_r^2}\left(1 - e^{-k^2\sigma_r^2}\right)\sqrt{P_cP_i} + \left(1 - e^{-k^2\sigma_r^2}\right)^2P_i \quad (59)$$

which shows that the bistatic geometry mixes the coherent and incoherent powers of the source/receiver subapertures. The exponent multiplying the coherent power is a factor of 2 smaller than that for monostatic, which implies that the coherency of a full bistatic aperture is less sensitive to radial position errors.

7.3. Comparison

The ensemble-averaged PTRs, (50) and (56), are plotted in Fig. 14 (top) for different σ_r and $N = 261$. Fig. 14 (middle) are the same computed numerically over random trials of the PTR sums averaged over 200 trials, which shows excellent agreement with the analytical expressions. In both cases, the resolution of the PTR does not change, but the coherent component drops very quickly with σ_r . Fig. 14 (bottom) are plots of the coherence loss at the PTR peak, $r = 0$, for different numbers of aperture points. When $\sigma_r = 0, P_i = 0$, there is only the coherent component. When $\sigma_r \approx \lambda/4$ the coherent component of the monostatic disappears and the power is entirely incoherent. When $\sigma_r \approx \lambda/2$ the bistatic power is entirely incoherent, which makes it slightly more resilient to position errors. This is due to the one-way phase error of each sensor, compared to the two-way phase error in the monostatic case. These show that, in order to limit the coherence loss of backprojected images, the radial position knowledge of the radar sensors for tomographic systems needs to be better than $\lambda/10$, and that a requirement of $\lambda/20$ is well-justified.

8. Backprojection of vector data

Here we derive an algorithm for backprojecting 3D vector data. While simple to implement, this ensures that different polarizations do not destructively interfere when summed coherently in free-space. In addition, this allows us to link the vector Born approximation in Section 2 to the scalar analyses in Sections 3,4,5,6 and 7. In Section 9, we test our algorithm on simulated scattered field measurements of dielectric point targets. A similar algorithm based on vectorial-induced current reconstruction was developed in Eyraud et al. (2013), and tested on a comet-analogue material in experiment Eyraud et al. (2018).

Assume that all four components of the S-matrix are measured by a fully-polarimetric bistatic radar system. Because \hat{v} and \hat{h} are orthogonal, any linear polarization can be synthesized as though it were transmitted or received. It is then possible to find a common polarization, $\hat{\beta}$, between any pair of incident and scattered directions, which is given by the cross product of the plane wave directions:

$$\hat{\beta} = \frac{\hat{k}_i \times \hat{k}_s}{|\hat{k}_i \times \hat{k}_s|} \quad (60)$$

Geometrically, $\hat{\beta}$ lies on the intersection of the planes containing the incident and scattered polarization vectors, shown in Fig. 15. Polarization synthesis is accomplished by projecting the components of the S-matrix onto $\hat{\beta}$ as

$$S_{is} = [\hat{\beta} \cdot \hat{v}_s \quad \hat{\beta} \cdot \hat{h}_s] \begin{bmatrix} S_{vv} & S_{vh} \\ S_{hv} & S_{hh} \end{bmatrix} \begin{bmatrix} \hat{v}_i \cdot \hat{\beta} \\ \hat{h}_i \cdot \hat{\beta} \end{bmatrix} \quad (61)$$

The action of polarization synthesis is equivalent to actively phasing a quad-pol radar system so that each radar on a pair of spacecraft orbiting a small body transmits and receives the linear polarization $\hat{\beta}$. This is also equivalent to two spacecraft, each with a single dipole antenna, where the dipoles of each radar are kept parallel to each other and parallel to $\hat{\beta}$. In Eyraud et al. (2018), only exact co-linear polarized data were used to generate images. (61) creates the co-linear polarization automatically from the full S-matrix.

The monochromatic vector backprojected image is computed as

$$V = \sum_{(i,s)} S_{is} e^{-i(\mathbf{k}_i - \mathbf{k}_s) \cdot \mathbf{x}} \quad (62)$$

where the phase of the S-matrix measurements is referenced to the origin. For monostatic systems, $\hat{k}_i \times \hat{k}_s = 0$ and (60) is indeterminate. If we desire to mix the monostatic S-matrix measurements, we can choose, for example,

$$\hat{\beta} = (\hat{v}_i + \hat{h}_i) / \sqrt{2} \quad (63)$$

From (6), the S-matrix for a point target at \mathbf{x}_p under the Born approximation is

$$\begin{bmatrix} S_{vv} & S_{vh} \\ S_{hv} & S_{hh} \end{bmatrix} = \begin{bmatrix} \hat{v}_s \cdot \hat{v}_i & \hat{v}_s \cdot \hat{h}_i \\ \hat{h}_s \cdot \hat{v}_i & \hat{h}_s \cdot \hat{h}_i \end{bmatrix} e^{i(\mathbf{k}_i - \mathbf{k}_s) \cdot \mathbf{x}_p} \quad (64)$$

The vector PTR is then found by substituting (64) into (61) and then into (62). However, it can be shown that

$$[\hat{\beta} \cdot \hat{v}_s \quad \hat{\beta} \cdot \hat{h}_s] \begin{bmatrix} \hat{v}_s \cdot \hat{v}_i & \hat{v}_s \cdot \hat{h}_i \\ \hat{h}_s \cdot \hat{v}_i & \hat{h}_s \cdot \hat{h}_i \end{bmatrix} \begin{bmatrix} \hat{v}_i \cdot \hat{\beta} \\ \hat{h}_i \cdot \hat{\beta} \end{bmatrix} = 1 \quad (65)$$

which means the vector PTR computed via (62) reduces to the scalar expression (16). This is expected because 1) the

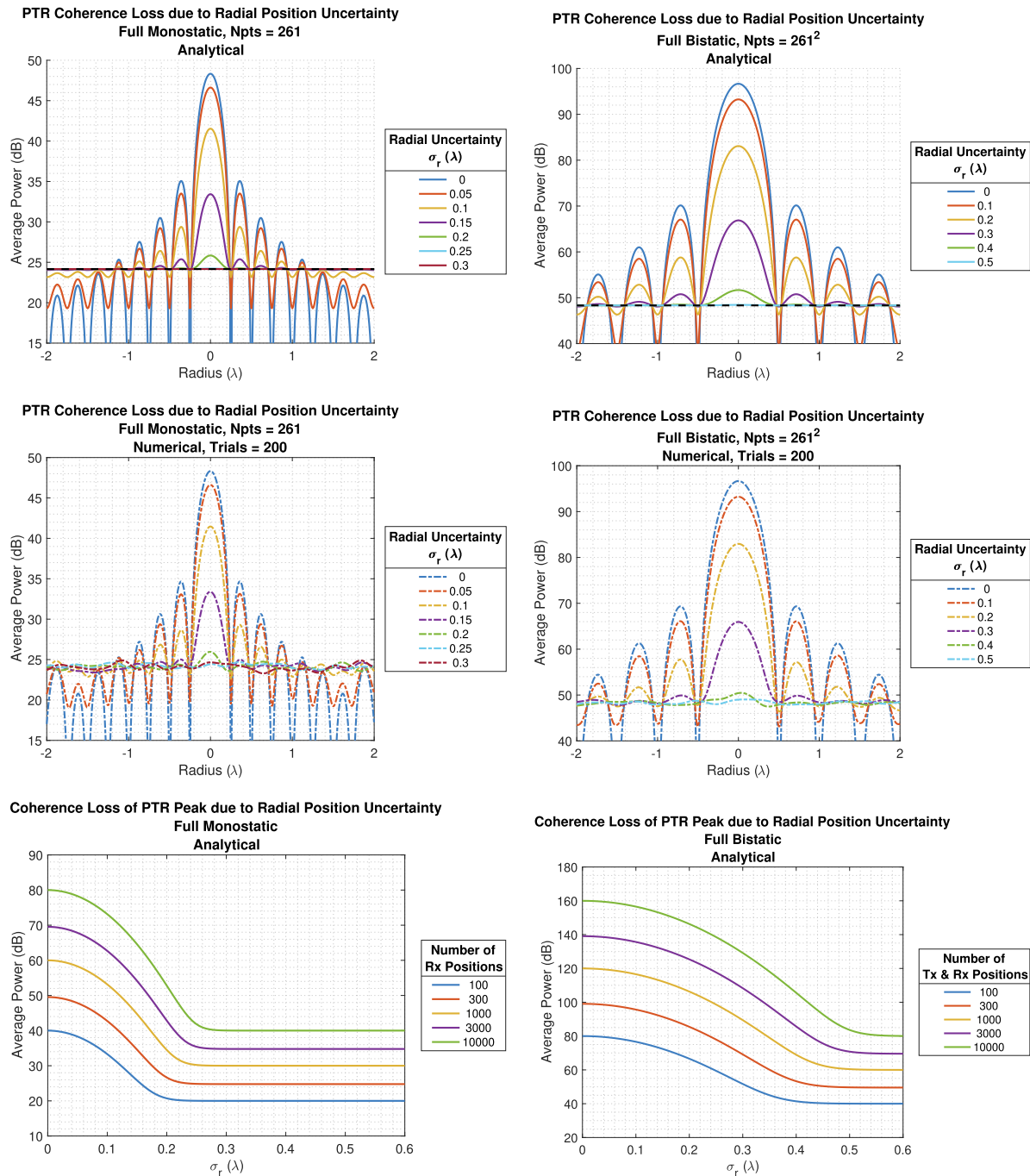


Fig. 14. Left column: coherence loss due to radial position uncertainty (i.e., error in the plane wave phase) for full monostatic. Left top: analytical (50)–(52). Left middle: numerical, (48). Left bottom: coherence loss of the PTR peak as a function of the standard deviation radial phase uncertainty, σ_r using (50). Right column: coherence loss due to radial position uncertainty for full bistatic. Right top: analytical (56)–(58). Right middle: numerical (53). Right bottom: coherent loss of PTR peak (56).

scattering of the BA is scalar and 2) the projection of the S-matrix through $\hat{\beta}$ collapses the vector decomposition.

9. Point target imaging

We test the vector backprojection algorithm using dielectric point targets, shown in Fig. 16. Each target is a dielectric sphere approximately $\lambda/45$ in diameter with a dielectric permittivity of $\epsilon_r = 2$ in a background of free-

space. The targets are spaced somewhat unevenly in the XY plane. The value of 2 was chosen only to give the targets contrast with the background. For widely-spaced sub-wavelength targets any choice of dielectric can be used to assess these algorithms.

Bistatic S-matrix measurements are simulated using the Method of Moments (MoM) solution of the vector VIE. The MoM has the advantage that it computes all combinations of incident and scattered directions for the same

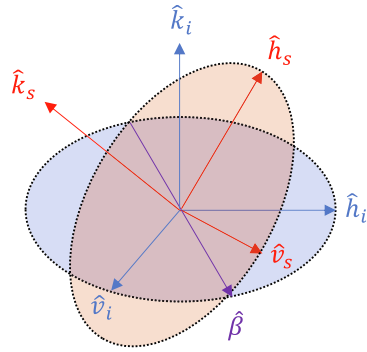


Fig. 15. Geometry showing the common polarization $\hat{\beta}$ between two bistatic measurement directions onto which the polarimetric S-matrix measurements can be projected to accomplish free-space backprojection of vector data.

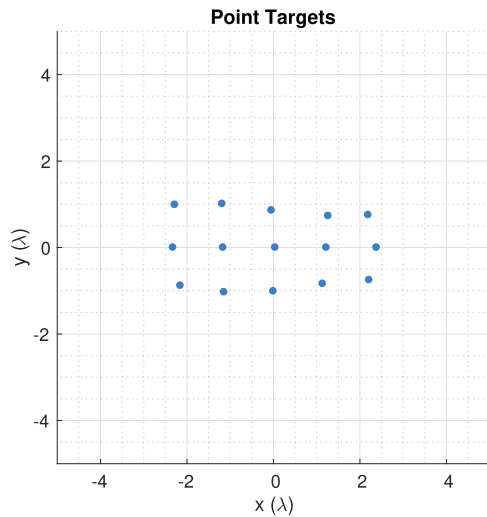


Fig. 16. Locations of dielectric point targets in the XY plane for the images in Fig. (17).

matrix inversion cost, which allows us to cleanly separate monostatic and bistatic geometries. The simulation contains no noise and the plane wave directions, phases, and polarizations are perfectly known. The incident/scattered field directions are simulated on a regular spherical grid at 3° steps in both θ and ϕ . The spherical grid of points is then subsampled to a disco ball approximation to avoid oversampling the polls.

Fig. 17 shows the imaging results for three sampling geometries and three sampling densities using the algorithm in Section 8. From left to right, the columns corresponds to the sampling density for a radius of convergence equal to $[1.6, 2.4, 4.8]\lambda$. For full monostatic and full bistatic geometries the boundary is depicted by a circle. For full k -space the boundary is a square, which is the Cartesian circulant boundary. The angular sampling step and total number of sampling points are given in Table 3. For k -space sampling, a single random set of

non-degenerate incident/scattered direction pairs are selected using the procedure in Section 6 and which are closest to measurements sampled on the 3° spherical grid.

Fig. 18 illustrates the effects of noise and coherent gain for the monostatic and full k -space configurations that have the highest sampling density. The maximum level of the S-matrix data in both cases is about -53 dB, while the mean level is around -70 dB. Noise is added to each complex S-matrix measurements as independent draws from a complex standard normal distribution

$$\gamma = \frac{\sqrt{P_n}}{\sqrt{2}}(N(0, 1) + iN(0, 1)) \quad (66)$$

where P_n is the noise power, and $N(0, 1)$ is a draw from a standard normal distribution with zero mean and unit variance. The noise level is chosen to be equal to the maximum signal value, $P_n = -53$ dB. Therefore, the signal to noise ratio (SNR) of all measurements is less than 0 dB and the SNR of roughly half of the measurements is less than -23 dB. These two examples are discussed in Section 10.2.

10. Discussion

10.1. Imaging results

The features and artifacts in the reconstructed images in Fig. 17 are consistent with the sampling geometries of spherical apertures and the use of monochromatic free-space focusing. All three geometries correctly focus on the point targets within the predicted radius of convergence. Recall, backprojection assumes that there is no intervening material between the sensors and the focal points. The sidelobes from the monostatic image do interfere somewhat and extend beyond the boundary of the collection of point targets. The bistatic image yielded the cleanest far sidelobes. The circulant repetitions of the k -space images fall precisely on the predicted Cartesian boundary.

10.2. Aperture gain of radar tomography systems

Fig. 18 illustrates free-space focusing in the presence of measurement noise. The noise level used is relatively high, where the SNR for all measurements is less than 0 dB. Still, the majority of point targets for the monostatic geometry are resolved and all the targets for the full k -space geometry are resolved. In both cases, the noise floor is above the level of the noise-free sidelobe levels. The gain over the noise is proportional to the number of coherent measurements. This is demonstrated by the improvement in the noise floor between the two geometries, where the k -space geometry has roughly 6 times as many sampling points as the monostatic case.

In general, spherical tomographic radar systems have the potential for very large aperture processing gains assuming all measurements can be collected. Airborne

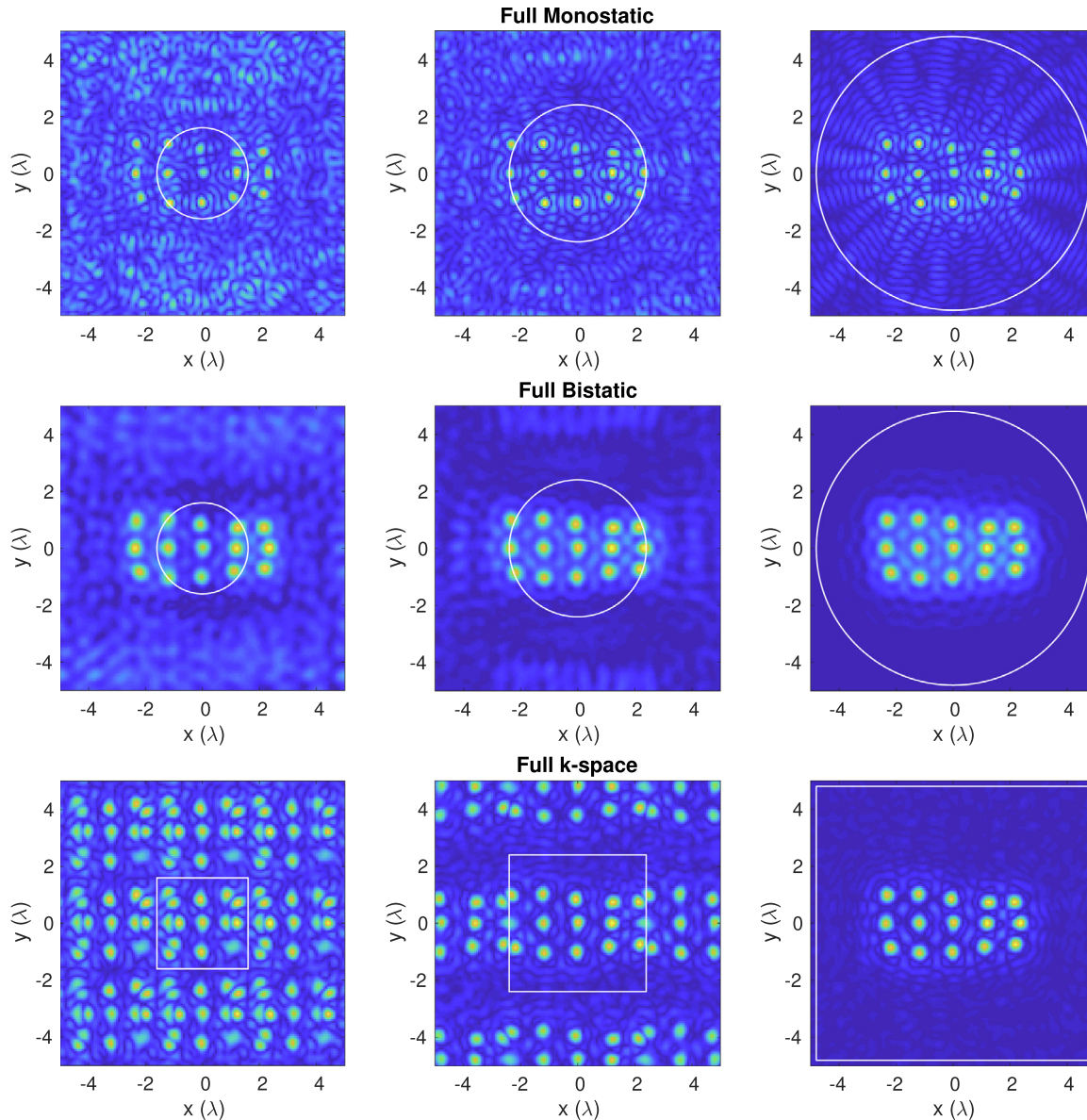


Fig. 17. Monochromatic free-space vector backprojection images of the point targets in Fig. 16 and sampling parameters in Table 3. Rows 1 through 3 are backprojection images for three sampling geometries: full monostatic, full bistatic, and full k -space. The images are displayed as normalized linear intensity from 0 to 1. Columns 1 through 3 corresponds to spherical sampling densities having radius of convergence of $[1.6, 2.4, 4.8]\lambda$, respectively. For monostatic and bistatic sampling the radius of convergence is represented by a white circle, while for k -space sampling the Cartesian circulant boundary is shown by a white square.

Table 3
Sampling Parameters for the Images in Fig. (17).

(λ)	Radius of Convergence		
	1.6	2.4	4.8
	Full Monostatic		
$\Delta\theta_{mono}$, Eq. (30)	$\sim 9^\circ$	$\sim 6^\circ$	$\sim 3^\circ$
N_{mono} , Eq. (36)	529	1177	4642
	Full Bistatic		
$\Delta\theta_{bi}$, Eq. (31)	$\sim 18^\circ$	$\sim 12^\circ$	$\sim 6^\circ$
$N_{bi,pairs}$, Eq. (38)	18769	91204	1385329
	Full k -space		
Δk ($1/\lambda$), Eq. (39)	~ 1.96	~ 1.31	~ 0.66
$N_{bi,pairs,k}$, Eq. (42)	1094	3707	29650

and space-borne SAR, including traditional orbital radar sounders, have aperture gains constrained by short observation times. Spherical apertures on the other hand can contribute thousands of measurements to a focal point, assuming the radar is sensitive to those interior points. This means that more and smaller low-power radar instruments could be used to achieve spatial coverage, while compensating signal-to-noise ratio through aperture gain.

10.3. Motivation of quad-pol radar systems for tomography

The choice of single-, dual-, or quad-pol radar architectures has implications for the cost and complexity of the

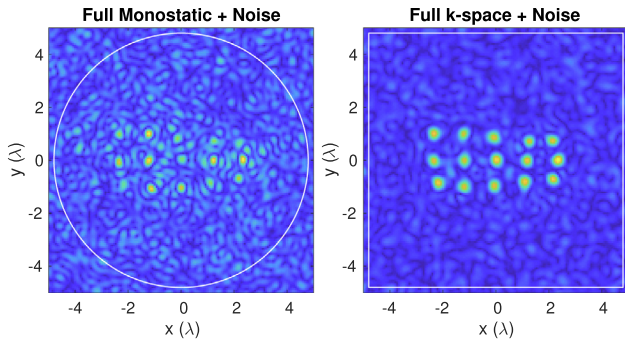


Fig. 18. Imaging examples with noisy data. Full monostatic (left) and full k -space (right) for the high density sampling (right column of Fig. 17). The noise level is equal to the maximum of all S-matrix measurements, so that the signal to noise ratio of all measurements is less than 0 dB and for half of all points it is worse than -20 dB.

radar, antenna design and mass, and future mission operations. The images above were formed using bistatic quad-pol S-matrix data in which a co-aligned incident/scattering polarization could always be constructed. This was motivated by the vector backprojection algorithm. In general, highly heterogeneous objects will depolarize the scattered field, beyond the capabilities of free-space algorithms to fully focus the data. There is also an architecture trade between having a slightly more complicated bistatic quad-pol radar system (requiring four times the data of single-pol systems) versus a single-pol bistatic experiment in which the antennas are kept co-aligned by the spacecraft. This level of coordination may be out of reach of current smallsat/cubesat flight systems, or be used to motivate needed capability. Finally, from the perspective of system robustness, a quad-pol radar system has built-in redundancy, should one half of the polarizations fail.

10.4. Feasibility of achieving full aperture sampling

We have shown that the total number of sampling points required to fully sample the monostatic and bistatic spherical apertures with monochromatic waves can be quite large. Monostatic apertures for low frequency radars (<20 MHz) can be completely sampled relatively easily with plausible mission durations, Sava and Asphaug (2018b); Sava and Asphaug (2018a). However, the number of bistatic pairs predicted by $N_{bi,pairs}$ for objects $d = 10\lambda$ is about 1 million, Fig. 11. The problem becomes worse for larger bodies and higher frequencies.

This raises an important question: are all bistatic pairs predicted by $N_{bi,pairs}$ required for high fidelity interior imaging? Recognizing that $N_{bi,pairs}$ was derived for monochromatic sampling, it is clear that wide-band, or multi-frequency, radar systems can obtain more information per sampling point, using the transmitter bandwidth to fill in more of k -space per sampling direction pair. However, the system bandwidth of low-frequency radars cannot be made arbitrarily large due to practical limitations of large antennas and so some spatial diversity is required. One

next step is to repeat these derivations for k -space filling assuming a finite bandwidth system. This will reduce the number of required bistatic measurements and should suggest optimal distributions of bistatic pairs for free-space focusing.

Finally, while free-space imaging methods are simple to implement, they do not use the scattered field information most efficiently. Inverse scattering methods formulate the imaging problem as an optimization in which each resolution cell of the 3D object dielectric is an unknown to be solved. It stands to reason that the true count of the number of unknowns in these problems is the number of k -space samples required to Nyquist sample the object, i.e., $N_{bi,pairs,k}$, (42). However, because the inverse scattering solution is non-unique, together with bistatic degeneracy in k -space, it is unclear how many or which bistatic pairs are optimally required to invert for the 3D object dielectric. In addition, regularization can effectively reduce the number of the degrees of freedom in the inversion, which reduces the apparent number of required bistatic measurements Haynes et al. (2012); Takala et al. (2018).

One hypothesis then is that the minimum number of bistatic measurements required for 3D imaging of small bodies is somewhere between $N_{bi,pairs,k}$ and $N_{bi,pairs}$. $N_{bi,pairs,k}$ quantifies the minimum k -space sampling of the object, and, while it contains no degenerate bistatic pairs, more measurements might be needed to address the non-uniqueness of the inverse scattering algorithms. $N_{bi,pairs}$, on the other hand, contains a large amount of redundant information across space and frequency, and therefore might be considered an upper bound. Because bistatic scattering information is almost certainly required for high quality imaging, and because the combinatoric computation of $N_{bi,pairs}$ for monochromatic waves predicts an unrealizable number of measurements, answering what is the minimum or optimal number of bistatic measurements, whether for free-space algorithms or 3D dielectric inversion, is an important topic of future investigation. In general, the interior make-up of the body does not change the required Doppler sampling rates, but only a large simulation study can answer definitively what is the minimum required sampling rate for more advanced inversion algorithms.

11. Conclusion

In this work, we derive angular sampling criteria for low-frequency 3D radar tomography systems for imaging the interiors of solar system small bodies. These results are intended to aid the design and analysis of radar tomography instruments and mission systems. We started with the vector Born approximation to derive and discuss the k -space interpretation of free-space scalar scattering, including the degeneracy of k -space measurements. We then derived the scalar point target response for monostatic, bistatic, and k -space sampling geometries in spherical

apertures. These were used to validate the angular sampling criteria and total number of spherical sampling points. We then derived expressions for aperture coherence loss in the presence of radial position errors, demonstrating the requirement for $\lambda/20$ position knowledge.

We derived a vector backprojection algorithm designed to combine quad-pol S-matrix measurements to form scalar images. We showed that with quad-pol data we can always find a co-aligned polarization between arbitrary bistatic measurement directions in order to collapse vector data into scalar images. We tested this algorithm on simulated S-matrix data of dielectric point targets. S-matrix data was generated with a source-independent electromagnetic simulator which allowed us to 1) generate the large number of source/receiver measurement pairs with a single scattering solution, and 2) cleanly test the image performance of monostatic versus bistatic sampling geometries.

In general, the predicted number of unique monochromatic bistatic measurement pairs for radar tomography of a small body grows very fast with body diameter and operating frequency. This has implications for how or whether all these measurements can be collected by practical radar systems. It also raises the question about whether all these measurements are ultimately required for wide-band systems or sophisticated imaging algorithms. This motivates future work to determine the minimum or optimal sets of measurements needed to successfully form 3D dielectric images of small bodies using inverse scattering algorithms, where, we expect, the number of spatial sampling points will most likely be less than those predicted for monochromatic imaging.

Declaration of Competing Interest

The authors declare that they have no known competing financial interests or personal relationships that could have appeared to influence the work reported in this paper.

Acknowledgments

A portion of this research was carried out at the Jet Propulsion Laboratory, California Institute of Technology, under a contract with the National Aeronautics and Space Administration (80NM0018D0004). © 2021. All rights reserved.

Appendix A. Fourier integral over the sphere

The surface integrals in (17) have the form

$$U = \int_{\Omega_k} e^{i\mathbf{k}\cdot\mathbf{x}} \sin \theta_k d\theta_k d\phi_k \quad (\text{A.1})$$

From symmetry the dot product is evaluated relative to a common fixed axis where $\mathbf{x} = \mathbf{r}$ is a radial vector and t is the angle between the vectors \mathbf{k} and \mathbf{r} so that $\mathbf{k} \cdot \mathbf{r} = kr \cos(t)$. Changing $\theta \rightarrow t$, the integral becomes

$$U = \int_0^{2\pi} \int_0^\pi e^{ikr \cos(t)} \sin t dt d\phi \quad (\text{A.2})$$

Using the identity

$$j_n(z) = \frac{(-i)^n}{2} \int_0^\pi e^{iz \cos \theta} P_n(\cos \theta) \sin \theta d\theta \quad (\text{A.3})$$

(A.2) evaluates to

$$U = 4\pi j_0(kr) = 4\pi \text{sinc}(kr) \quad (\text{A.4})$$

where $j_n(x)$ is the spherical Bessel function, and $\text{sinc}(x) = \sin(x)/x$. The following derivative is useful for finding the locations of the sidelobe peaks

$$\frac{d}{dx} \text{sinc}(ax) = \frac{ax \cos(ax) - \sin(ax)}{ax^2} \quad (\text{A.5})$$

Appendix B. Doppler sampling

The geometry is shown in Fig. 7. The body radius is a and the sensor altitude above the body-enclosing sphere is h . The target at the limb is located at

$$\mathbf{x} = a \sin \beta \hat{x} + a \cos \beta \hat{y} \quad (\text{B.1})$$

where

$$\cos \beta = \frac{a}{a+h} \quad (\text{B.2})$$

The sensor positions in a circular orbit are

$$\mathbf{s}_1 = (a+h) \hat{y} \quad (\text{B.3})$$

$$\mathbf{s}_2 = (a+h) \sin \theta \hat{x} + (a+h) \cos \theta \hat{y} \quad (\text{B.4})$$

The ranges from the sensor points to the target at the limb are then

$$r_1 = |\mathbf{s}_1 - \mathbf{x}| \quad (\text{B.5})$$

$$= \sqrt{(a+h)^2 - a^2} \quad (\text{B.6})$$

$$r_2 = |\mathbf{s}_2 - \mathbf{x}| \quad (\text{B.7})$$

$$= \sqrt{((a+h) \sin \theta - a \sin \beta)^2 + ((a+h) \cos \theta - a \cos \beta)^2} \quad (\text{B.8})$$

$$= \sqrt{h^2 - 2a(a+h)(\sin \theta \sin \beta + \cos \theta \cos \beta - 1)} \quad (\text{B.9})$$

The difference of the two-way phases under monostatic operation is

$$\Delta\phi_{2\text{-way,mono}} = 2\phi_1 - 2\phi_2 \quad (\text{B.10})$$

$$= 2k(r_1 - r_2) \quad (\text{B.11})$$

While the ‘two-way’ phase change for bistatic operation is

$$\Delta\phi_{2\text{-way,bi}} = 2\phi_1 - (\phi_1 + \phi_2) \quad (\text{B.12})$$

$$= k(r_1 - r_2) \quad (\text{B.13})$$

Assuming that the change in angle is small, $\sin \theta \ll 1$, or that $h \gg a$, it can be shown that

$$r_1 - r_2 \approx a \sin \theta \quad (\text{B.14})$$

which is the same result as plane-wave far-approximation with the limb equal to the point $x = a$. Using this approximation the change in phase can be approximated

$$\Delta\phi_{2\text{-way,mono}} \approx 2ka \sin \theta \approx 2ka\theta \tag{B.15}$$

$$\Delta\phi_{2\text{-way,bi}} \approx ka \sin \theta \approx ka\theta \tag{B.16}$$

Alternately, we can solve for θ exactly for a given $\Delta\phi$. Starting with

$$pk(r_1 - r_2) = \Delta\phi \tag{B.17}$$

where $p = [1, 2]$, substituting (B.9) and solving for θ , we get

$$\theta = \beta - \arccos\left(\frac{h^2 - \left(r_1 - \frac{\Delta\phi}{pk}\right)^2}{2a(a+h)} + 1\right) \tag{B.18}$$

Setting $z = h/a$ (B.18) can be written

$$\theta = \beta - \arccos\left(\frac{\frac{\Delta\phi\sqrt{z^2+2z}}{pka} - \frac{(\Delta\phi)^2}{2(pk a)^2} + 1}{(1+z)}\right) \tag{B.19}$$

It can be shown that when $z > 0.2$ or $a/\lambda > 2$ that this is well-approximated by

$$\theta \approx \frac{\Delta\phi}{pka} \tag{B.20}$$

which is equivalent to the result above.

Appendix C. Plane wave spherical harmonic content and spherical quadrature

The far-field angular sampling step for tomography can also be derived by considering the spherical harmonic content of the plane wave expansion at a radius r and quadrature sampling of the Fourier surface integral. The expansion of a scalar plane wave in terms spherical harmonics at the origin is, Tsang et al. (2000),

$$e^{i\mathbf{k}\cdot\mathbf{x}} = \sum_{l=0}^{\infty} \sum_{m=-l}^l i^l j_l(kr) Y_{lm}(\theta, \phi) Y_{lm}^*(\theta_k, \phi_k) \tag{C.1}$$

where (θ_k, ϕ_k) are the spherical coordinates of the wavevector direction \mathbf{k} and (r, θ, ϕ) are the coordinates of the observation point \mathbf{x} . Substituting this into (A.1),

$$U = 4\pi k^2 \sum_{l=0}^{\infty} \sum_{m=-l}^l i^l j_l(kr) Y_{lm}(\theta, \phi) \int_{\Omega_k} Y_{lm}^*(\theta_k, \phi_k) \times \sin \theta_k d\theta d\phi_k \tag{C.2}$$

For a fixed kr , the spherical Bessel function only has harmonic content up to a maximum degree L , which is given approximately as, Yaghjian (1996),

$$L \approx \left\lceil 1.1kr \left(1 + \frac{1}{kr}\right) \right\rceil \tag{C.3}$$

This allows the sum in (C.2) to be truncated at L . Next, to ensure convergence of the harmonic sum (C.2), the surface integral over Ω_k is computed over a discrete number of plane wave directions (θ_k, ϕ_k) . The integration is done by using $N_\theta = \lceil (L+1)/2 \rceil$ Gaussian-Legendre quadrature points in θ and $N_\phi = L+1$ trapezoidal integration points in ϕ at each θ . In this scheme, the poles are oversampled, and the quadrature steps in θ are almost evenly spaced but never sample the poles. Dividing $N_\theta + 1$ into π , or using the ϕ step at the equator, the angular sampling to integrate exactly a spherical harmonic of degree L is approximately

$$\Delta\theta = \frac{2\pi}{L+1} \tag{C.4}$$

Substituting (C.3) and ignoring the rounding

$$\Delta\theta \approx \frac{2\pi}{1.1kr\left(1 + \frac{1}{kr}\right) + 1} \tag{C.5}$$

Further assuming that $r/\lambda \gg 1$ we get

$$\Delta\theta \approx \frac{\lambda}{1.1r} \tag{C.6}$$

In summary, the integral (A.1) can be computed exactly over discrete samples of plane wave directions by choosing an angular step consistent with the quadrature rules for integration for spherical harmonics of degree L , where L is determined by the harmonic content at the observation radius.

This derivation assumed a single factor of kr in the exponential of the PTR integral (A.1), and therefore applies to bistatic and fixed transmit geometries. For monostatic, the argument of the spherical Bessel function in (C.1) will be $2kr$, and therefore (C.6) needs an additional factor of $1/2$.

Appendix D. Ensemble average of a sum of wave functions

We derive the average power of a sum of wave functions with Gaussian random phases. The voltage signal is, generally,

$$V = \sum_m \psi_m e^{isz_m} \tag{D.1}$$

where ψ_m is a wave function, z_m are IID Gaussian random variables with zero mean and standard deviation σ , and s is real-valued. The average power is computed as

$$P = |V|^2 = VV^* \tag{D.2}$$

$$= \left(\sum_m \psi_m e^{isz_m} \right) \left(\sum_{m'} \psi_{m'}^* e^{-isz_{m'}} \right) \tag{D.3}$$

$$= \sum_{m,m'} \psi_m \psi_{m'}^* e^{i(sz_m - sz_{m'})} \tag{D.4}$$

When $m = m'$, the random phase is zero and the self-terms should not be included in the ensemble average. The ensemble average is then brought inside the double sum to the random phases as

$$P = \sum_m |\psi_m|^2 + \sum_{m,m',m \neq m'} \psi_m \psi_{m'}^* e^{i(sz_m - sz_{m'})} \quad (D.5)$$

$$= \sum_m |\psi_m|^2 + \sum_{m,m',m \neq m'} \psi_m \psi_{m'}^* e^{i(sz_m - sz_{m'})} \quad (D.6)$$

Assuming the random variables are independent but with identical variance for each index, we use the characteristic function, Appendix E, and this becomes

$$P = \sum_m |\psi_m|^2 + e^{-s^2\sigma^2} \sum_{m,m',m \neq m'} \psi_m \psi_{m'}^* \quad (D.7)$$

Next, add and subtract the sum of self-terms multiplied by the exponential

$$P = \sum_m |\psi_m|^2 + e^{-s^2\sigma^2} \sum_{m,m',m \neq m'} \psi_m \psi_{m'}^* + e^{-s^2\sigma^2} \sum_m |\psi_m|^2 - e^{-s^2\sigma^2} \sum_m |\psi_m|^2 \quad (D.8)$$

The positive term is used to complete the double sum after which this can be rearranged as

$$P = e^{-s^2\sigma^2} \sum_{m,m'} \psi_m \psi_{m'}^* + \left(1 - e^{-s^2\sigma^2}\right) \sum_m |\psi_m|^2 \quad (D.9)$$

The double sum is the unperturbed, or mean-field, coherent component of the power, P_c . The sum of the magnitude squared is the total incoherent power, P_i , contributed by the random variation. Therefore,

$$P = e^{-s^2\sigma^2} P_c + \left(1 - e^{-s^2\sigma^2}\right) P_i \quad (D.10)$$

$$P_c = \sum_{m,m'} \psi_m \psi_{m'}^* = \left| \sum_m \psi_m \right|^2 \quad (D.11)$$

$$P_i = \sum_m |\psi_m|^2 \quad (D.12)$$

This result is similar to the expressions in Carrer et al. (2019) for arrays of smallsat radar sounders with position errors.

Appendix E. Characteristic function

The characteristic function for a multivariate Gaussian random variable $\mathbf{z} \sim N(\boldsymbol{\mu}, \boldsymbol{\Sigma})$ is given generally as, Scarowsky (1973, Eq. 2.22),

$$E[e^{i\mathbf{s}'\mathbf{z}}] = e^{i\boldsymbol{\mu}'\mathbf{s} - \frac{1}{2}\mathbf{s}'\boldsymbol{\Sigma}\mathbf{s}} \quad (E.1)$$

For two zero-mean random variables with correlation C this is

$$e^{i(k_1 z_1 + k_2 z_2)} = e^{-\frac{1}{2}(k_1^2 \sigma_1^2 + 2Ck_1 k_2 \sigma_1 \sigma_2 + k_2^2 \sigma_2^2)} \quad (E.2)$$

References

Arumugam, D.D., Gim, Y., Heggy, E., Wu, X., 2018. Synthetic aperture radar imaging of the interior of comets using time-domain back-projection. In: 2018 IEEE International Symposium on Antennas and Propagation & USNC/URSI National Radio Science Meeting. IEEE, pp. 1795–1796.

Asphaug, E., Belton, M., Bockelee-Morvan, D., Chesley, S., Delbo, M., Farnham, T., Gim, Y., Grimm, R., Herique, A., Kofman, W. et al., 2014. The Comet Radar Explorer Mission. In: DPS, pp. 209–07)

Bambach, P., Deller, J., Vilenius, E., Pursiainen, S., Takala, M., Braun, H. M., Lentz, H., Wittig, M., 2018. DISCUS—the deep interior scanning cubesat mission to a rubble pile near-Earth asteroid. Adv. Space Res. 62 (12), 3357–3368.

van den Berg, P.M., Van Broekhoven, A., Abubakar, A., 1999. Extended contrast source inversion. Inverse Problems 15 (5), 1325.

Carrer, L., Gerekos, C., Bovolo, F., Bruzzone, L., 2019. Distributed radar sounder: A novel concept for subsurface investigations using sensors in formation flight. IEEE Trans. Geosci. Remote Sens. 57 (12), 9791–9809.

Chew, W.C., 1995. Waves and fields in inhomogeneous media, vol. 522. IEEE Press, New York.

Chew, W.C., Wang, Y.-M., 1990. Reconstruction of two-dimensional permittivity distribution using the distorted Born iterative method. IEEE Trans. Medical Imaging 9 (2), 218–225.

Devaney, A., 1984. Geophysical diffraction tomography. IEEE Trans. Geosci. Remote Sens. 1, 3–13.

Eyraud, C., Hérique, A., Geffrin, J.-M., Kofman, W., 2018. Imaging the interior of a comet from bistatic microwave measurements: case of a scale comet model. Adv. Space Res. 62 (8), 1977–1986.

Eyraud, C., Vaillon, R., Litman, A., Geffrin, J.-M., Merchiers, O., 2013. Polarization effects in 3D vectorial-induced current reconstructions. JOSA A 30 (10), 1967–1974.

Fortuny-Guasch, J., Lopez-Sanchez, J.M., 2001. Extension of the 3-D range migration algorithm to cylindrical and spherical scanning geometries. IEEE Trans. Antennas Propag. 49 (10), 1434–1444.

Gim, Y., Heggy, E., Arumugam, D., Wu, X., Asphaug, E.I., 2014. 3D synthetic aperture radar imaging of the interior of the cometary nucleus. AGUFM 2014, P51C–3962.

Goldberg, H., Karatekin, Ö., Ritter, B., Herique, A., Tortora, P., Prioroc, C., Gutierrez, B.G., Martino, P., Carnelli, I., Garcia, B., 2019. The Juventas cubesat in support of ESA’s Hera mission to the asteroid Didymos. In: Small Satellite Conference, Logan, Utah.

Granados, R., Herique, A., Rochat, E., et al., 2018. Long term simulations for bi-static radar and test bench design. In: 2018 European Frequency and Time Forum (EFTF). IEEE, pp. 225–230.

Greene, C., Moller, R., 1962. The effect of normally distributed random phase errors on synthetic array gain patterns. IRE Trans. Military Electron. 2, 130–139.

Hansen, J.E., 1988. Spherical near-field antenna measurements volume 26. Iet.

Haynes, M., Clarkson, S., Moghaddam, M., 2012. Electromagnetic inverse scattering algorithm and experiment using absolute source characterization. IEEE Trans. Antennas Propagat. 60 (4), 1854–1867.

Haynes, M., Virkki, A., Venditti, F., Hickson, D., Pinilla-Alonso, N., Brisset, J., Benner, L., Raymond, C., Lazio, J., Freeman, A. et al., 2020. Asteroids inside out: Radar tomography, community white paper for the planetary decadal survey, 2023–2032.

Hérique, A., Agnus, B., Asphaug, E., Barucci, A., Beck, P., Bellerose, J., Biele, J., Bonal, L., Bousquet, P., Bruzzone, L., et al., 2018. Direct observations of asteroid interior and regolith structure: science measurement requirements. Adv. Space Res. 62 (8), 2141–2162.

Hérique, A., Kofman, W., Beck, P., Bonal, L., Buttarazzi, I., Heggy, E., Lasue, J., Levasseur-Regourd, A.C., Quirico, E., Zine, S., 2016. Cosmochemical implications of CONSERT permittivity characterization of 67P/CG. Mon. Not. R. Astron. Soc. 462 (Suppl_1), S516–S532.

Herique, A., Plettemeier, D., Goldberg, H., Kofman, W., 2020. JuRa: the Juventas Radar on Hera to fathom Didymoon. In: European Planetary Science Congress, pp. EPSC2020-595.

- Hérique, A., Plettemeier, D., Lange, C., Grundmann, J.T., Ciarletti, V., Ho, T.-M., Kofman, W., Agnus, B., Du, J., Fa, W., et al., 2019. A radar package for asteroid subsurface investigations: Implications of implementing and integration into the MASCOT nanoscale landing platform from science requirements to baseline design. *Acta Astronaut.* 156, 317–329.
- Knaell, K., Cardillo, G., 1995. Radar tomography for the generation of three-dimensional images. *IEEE Proc.-Radar, Sonar Navigat.* 142 (2), 54–60.
- Kofman, W., Hérique, A., Barbin, Y., Barriot, J.-P., Ciarletti, V., Clifford, S., Edenhofer, P., Elachi, C., Eyraud, C., Goutail, J.-P., et al., 2015. Properties of the 67P/Churyumov-Gerasimenko interior revealed by CONSERT radar. *Science* 349 (6247).
- Kofman, W., Hérique, A., Goutail, J.-P., Hagfors, T., Williams, I., Nielsen, E., Barriot, J.-P., Barbin, Y., Elachi, C., Edenhofer, P., et al., 2007. The Comet Nucleus Sounding Experiment by Radiowave Transmission (CONSERT): A short description of the instrument and of the commissioning stages. *Space Sci. Rev.* 128 (1–4), 413–432.
- Kofman, W., Safaeinili, A., 2004a. Peering inside near-earth objects with radio tomography. *Mitigation of hazardous comets and asteroids*, p. 201.
- Kofman, W., Safaeinili, A., 2004b. Radar techniques applied to subsurface studies in solar system exploration. In: *Tools and Technologies for Future Planetary Exploration*, vol. 543, pp. 39–50.
- Kong, J.A., 1986. *Electromagnetic Wave Theory*. Wiley.
- Michel, P., Küppers, M., Carnelli, I., 2018. The Hera mission: European component of the ESA-NASA AIDA mission to a binary asteroid. *cosp.* 42, B1–1.
- Ono, T., Oya, H., 2000. Lunar Radar Sounder (LRS) experiment onboard the SELENE spacecraft. *Earth, Planets Space* 52 (9), 629–637.
- Picardi, G., Biccari, D., Seu, R., Plaut, J., Johnson, W., Jordan, R., Safaeinili, A., Gurnett, D., Huff, R., Orosei, R. et al., 2004. MARSIS: Mars advanced radar for subsurface and ionosphere sounding. In: *Mars Express: The Scientific Payload*, vol. 1240, pp. 51–69.
- Pursiainen, S., Kaasalainen, M., 2016. Orbiter-to-orbiter tomography: a potential approach for small solar system bodies. *IEEE Trans. Aerosp. Electron. Syst.* 52 (6), 2747–2759.
- Richards, M.A., Scheer, J., Holm, W.A., Melvin, W.L., 2010. *Principles of modern radar*. Citeseer.
- Safaeinili, A., Gulkis, S., Hofstadter, M., Jordan, R., 2002. Probing the interior of asteroids and comets using radio reflection tomography. *Meteoritics Planet. Sci.* 37 (12), 1953–1963.
- Sava, P., Asphaug, E., 2018a. 3D radar wavefield migration of comet interiors. *Adv. Space Res.* 62 (5), 1146–1164.
- Sava, P., Asphaug, E., 2018b. 3D radar wavefield tomography of comet interiors. *Adv. Space Res.* 61 (8), 2198–2213.
- Scarowsky, I., 1973. *Quadratic forms in normal variables* Ph.D thesis. McGill University.
- Seu, R., Phillips, R.J., Biccari, D., Orosei, R., Masdea, A., Picardi, G., Safaeinili, A., Campbell, B.A., Plaut, J.J., Marinangeli, L., et al., 2007. SHARAD sounding radar on the Mars Reconnaissance Orbiter. *J. Geophys. Res.: Planets* 112 (E5).
- Sorsa, L.-I., Takala, M., Bambach, P., Deller, J., Vilenius, E., Pursiainen, S., 2019. Bistatic full-wave radar tomography detects deep interior voids, cracks, and boulders in a rubble-pile asteroid model. *Astrophys. J.* 872 (1), 44.
- Takala, M., Bambach, P., Deller, J., Vilenius, E., Wittig, M., Lentz, H., Braun, H.M., Kaasalainen, M., Pursiainen, S., 2018. Far-field inversion for the deep interior scanning cubesat. *IEEE Trans. Aerosp. Electron. Syst.* 55 (4), 1683–1697.
- Tsang, L., Kong, J., Ding, K., 2000. *Scattering of electromagnetic waves. Theory and Applications*, vol. 1. Wiley Interscience, New York.
- Tsang, L., Kong, J.A., Shin, R.T., 1985. *Theory of microwave remote sensing*. Wiley Interscience, New York.
- Yaghjian, A.D., 1996. Sampling criteria for resonant antennas and scatterers. *J. Appl. Phys.* 79 (10), 7474–7482.